arXiv:0710.0008v1 [physics.chem-ph] 28 Sep 2007

Dissociative electron attachment to the H_2O molecule. I. Complex-valued potential-energy surfaces for the $^2B_1$, $^2A_1$, and $^2B_2$ metastable states of the water anion

Daniel J. Haxton,[1,2,*] C. W. McCurdy,[2,3] and T. N. Rescigno[2]

[1]*Department of Chemistry, University of California, Berkeley, California 94720*
[2]*Lawrence Berkeley National Laboratory, Chemical Sciences, Berkeley, California 94720*
[3]*Departments of Applied Science and Chemistry, University of California, Davis, California 95616*

We present the results of calculations defining global, three-dimensional representations of the complex-valued potential-energy surfaces of the $^2B_1$, $^2A_1$, and $^2B_2$ metastable states of the water anion that underlie the physical process of dissociative electron attachment to water. The real part of the resonance energies is obtained from configuration-interaction calculations performed in a restricted Hilbert space, while the imaginary part of the energies (the widths) is derived from complex Kohn scattering calculations. A diabatization is performed on the $^2A_1$ and $^2B_2$ surfaces, due to the presence of a conical intersection between them. We discuss the implications that the shapes of the constructed potential-energy surfaces will have upon the nuclear dynamics of dissociative electron attachment to H_2O.

PACS numbers: 34.80.Ht

I. INTRODUCTION

Dissociative electron attachment (DEA) to the water molecule proceeds through a number of channels, each with a different energetic threshold,

$$H_2O + e^- \rightarrow \begin{cases} H + OH^- & 3.27\ \text{eV} \\ H_2 + O^- & 3.56\ \text{eV} \\ H^- + OH \quad (X\ ^2\Pi) & 4.35\ \text{eV} \\ H + H + O^- & 8.04\ \text{eV} \\ H^- + OH^* \quad (^2\Sigma) & 8.38\ \text{eV} \\ H^- + H + O & 8.75\ \text{eV} \end{cases} \quad (1)$$

The production of these species occurs via three metastable Born-Oppenheimer electronic states of the H_2O^- system, whose vertical transition energies therefore determine the incident energies at which DEA occurs. Those electronic states of the anion are the $^2B_1$, $^2A_1$, and $^2B_2$ Feshbach resonances, and they are responsible for the three distinct peaks in the DEA cross section. Their potential-energy surfaces contain asymptotes corresponding to the product channels listed in Eq.(1), with the exception of the H+OH^- channel; this product is a result of nonadiabatic effects.

Here we report the construction of the complex-valued adiabatic potential-energy surfaces associated with these resonance states, which will be used within the local complex potential (LCP) model [1, 2, 3, 4, 5] to calculate the nuclear dynamics leading to dissociation. The present study is followed by a second paper[6], to which we will refer as paper II, in which we present the results of nuclear dynamics calculations under the LCP model using the calculated surfaces.

Dissociative electron attachment to water was studied as early as 1930, in the experiment of Lozier[7], and as recently as 2006, in the study by Fedor *et al.*[8]. These two experiments, along with the rest of the prior theoretical and experimental work on this subject[9, 10, 11, 12, 13, 14, 15, 16, 17, 18, 19, 20, 21], have succeeded in characterizing each of the product channels of Eq.(1) and the three Feshbach resonances involved in their production. However, prior to our recent theoretical study of DEA to water via the lowest-energy $^2B_1$ resonance[22, 23], there had been no complete theoretical treatment of this process, nor, in fact, any *ab initio* treatment of dissociative attachment to any molecule, involving more than one nuclear degree of freedom. We will give a more complete summary of the prior theoretical and experimental results concerning the dynamics of this process in paper II.

The present treatment supersedes our previous study of DEA via the lowest-energy $^2B_1$ state. We have also studied the angular dependence of DEA to H_2O and H_2S via the $^2B_1$ state of either anion [24]. Additionally, we previously presented a qualitative study of the topology of the potential-energy surfaces of these three electronic states [25], including the many intersections that these surfaces exhibit. That qualitative study informs the present study, in which we construct quantitative surfaces.

Two of the most significant features of these surfaces can be seen in Fig. 1, reproduced here from Ref.[25]. This figure depicts the behavior of the resonance energies with respect to the H-O-H bending angle θ_{HOH}, fixing the OH bond lengths at r_1=r_2=1.81a_0. The $^2B_1$ and $^2A_1$ resonances are degenerate at linear geometry; this degeneracy will lead to Renner-Teller coupling between the two states. In addition, there is a conical intersection between the $^2A_1$ and $^2B_2$ surface located at approximately θ_{HOH}=73°. This conical intersection plays a crucial role for the nuclear dynamics of DEA via the uppermost $^2B_2$

*Present address: Department of Physics and JILA, University of Colorado, Boulder, CO 80309, USA.

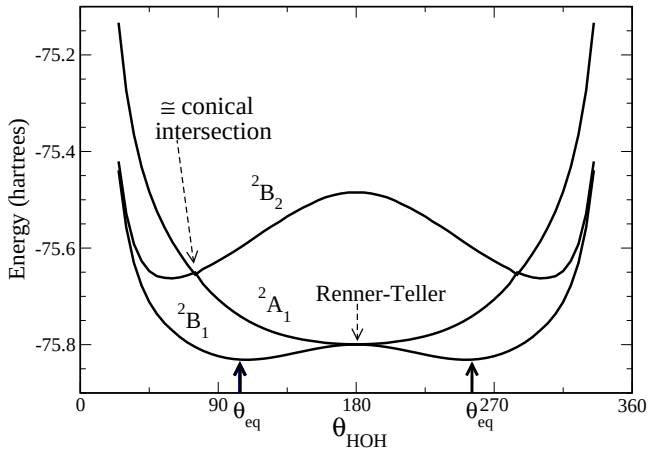

FIG. 1: Real parts of resonance energies, in units of hartrees, for OH bond distance = $1.81a_0$ in C_{2v} geometry, plotted with respect to bending angle, in degrees.

resonance state.

The presence of a conical intersection between the adiabatic $^2A_1$ and $^2B_2$ states means that the nuclear dynamics calculations that employ these potential-energy surfaces must either explicitly include the coupling between them, or be performed in a diabatic basis with a smooth coupling term. We perform an approximate diabatization of the calculated adiabatic $^2A_1$ and $^2B_2$ (1 and 2 $^2A'$) states to produce diabatic $^2A_1$ and $^2B_2$ surfaces. This diabatization is based upon the diagonalization of a particular symmetry operation described in Sec. V C, not the explicit minimization of derivative matrix elements.

A resonance state may be characterized by a width, Γ, and an energy, E_R, which are functions of the internuclear geometry $\vec{q}$. These quantities define a complex potential surface $V(\vec{q})$,

$$V(\vec{q}) = E_R(\vec{q}) - i\frac{\Gamma(\vec{q})}{2}. \qquad (2)$$

The width Γ is related to the lifetime as $\tau = 1/\Gamma$ (we use atomic units throughout). For a triatomic, the internal coordinates $\vec{q}$ may be the set of bond-angle coordinates (r_1, r_2, θ).

We use separate techniques to define the two components of the potential-energy surfaces, $E_R(\vec{q})$ and $\Gamma(\vec{q})$. We employ the complex Kohn variational method [26, 27, 28, 29, 30, 31, 32, 33, 34, 35] to perform scattering calculations which include the effect of the electronic continuum upon the anion state. These calculations yield both E_R and Γ, but we discard the value of E_R obtained from them. In its place, we use bound-state configuration-interaction (CI) calculations to obtain E_R.

In the asymptotic regions, the resonances become bound electronic states, and therefore the use of bound-state methods is entirely appropriate in those regions of nuclear geometry. Near the Franck-Condon region where these states are resonances, our CI treatment restricts the included configuration space to eliminate the ground state electronic continuum from the calculation. Thus our CI calculations neglect the shift in E_R due to coupling with that continuum, a well-known effect explained by the Feshbach resonance formalism [36]. Since the shift in E_R by this coupling is generally of the same order as the width, Γ, this is an excellent approximation in regions where the resonance is narrow. The three resonance states we treat here have as their dominant configuration an electron attached to a singly excited configuration of the neutral target (Feshbach resonances), and thus tend to have small widths. However, there are a some geometries where the width of one or the other of the two upper resonances is of the order of a few tenths of an eV, and in those regions the error in our calculated values of E_R for that resonance are larger.

We also define a ground-state neutral H_2O potential surface. The resulting energetics of the anion surfaces relative to the ground state appear to reproduce the vertical transition energies and all but one of the two-body asymptotes of these resonances very well, without a relative vertical adjustment between the neutral and anion calculations. However, as we will describe in detail, the CI calculations fail to produce one of the two-body breakup asymptotes on one resonance surface, and we are forced to employ an *ad hoc* patching procedure with another CI to correct the unphysical behavior. A similar patching procedure was necessary to correctly describe the three body breakup asymptotes, but dynamics leading to them is not part of the study we will present in paper II.

The data points calculated at a large set of nuclear geometries are assembled into global representations of the potential-energy surfaces. We construct the global representations of the real part, E_R, and the width, Γ, separately. The global representations of the real parts of the adiabatic $^2B_1$ and the diabatic $^2A_1$ and $^2B_2$ surfaces are defined by a sum of an analytic fit and a spline of the residual error of this fit. We also define a global representation of the off-diagonal coupling between the diabatic states. The global representations of E_R for the adiabatic $^2A_1$ and $^2B_2$ states are obtained as the eigenvalues of the 2×2 Hamiltonian matrix defined by the fitted diabatic surfaces. The adiabatic-to-diabatic transformation angle is applied to the constructed width surfaces to obtain diabatic widths. The final result is a complete set of complex potential surfaces for the full dynamics calculations we report in paper II.

The outline of this paper is as follows. We begin in Sec. II with a description of the electronic structure of the resonance states and the basic features of their potential-energy surfaces, reviewing the results on the topology of those surfaces of Ref. [25]. In Sec. III we discuss the complex Kohn scattering calculations from which we obtain $\Gamma(\vec{q})$, present the results of these calculations, and describe the construction of the global potential-energy surfaces from the individual data points. In Sec. V we do the same for the configuration-interaction calculations

defining $E_R(\vec{q})$. In Sec. VI we present the constructed potential-energy surfaces and discuss their features.

II. ELECTRONIC STRUCTURE OF THE RESONANCE STATES

The electronic states that are primarily involved in dissociative electron attachment to H_2O are the $^2B_1$, $^2A_1$, and $^2B_2$ Feshbach resonances [7, 8, 9, 10, 11, 12, 13, 14, 15, 16, 17, 18, 19, 20, 21, 22, 23, 24, 25]. At the equilibrium geometry of neutral H_2O, $r_1 = r_2 = 1.81a_0$, $\theta = 104.5°$, where a_0 is the Bohr radius $0.529189379 \times 10^{-10}$ m, these states are characterized by their dominant electronic configurations

$$^2B_1: \quad 1a_1^2\ 2a_1^2\ 1b_2^2\ 3a_1^2\ 1b_1^1\ 4a_1^2$$

$$^2A_1: \quad 1a_1^2\ 2a_1^2\ 1b_2^2\ 3a_1^1\ 1b_1^2\ 4a_1^2$$

$$^2B_2: \quad 1a_1^2\ 2a_1^2\ 1b_2^1\ 3a_1^2\ 1b_1^2\ 4a_1^2$$

such that each is described as $[H_2O]^{-1}4a_1^2$. The parent state of each corresponds to the analagous configuration $[H_2O]^{-1}4a_1^1$, which may be a singlet or a triplet. Since the resonance states are doublets, both the singlet and triplet states of the neutral may be considered the parent state to which the incident electron is attached.

The peaks in the DEA cross section occur at approximately 6.5, 8.4, and 11.8eV, respectively, at the equilibrium geometry of the neutral; these values approximate the vertical transition energies of the resonances. The ionization energy of H_2O is 12.621eV. The vertical transition energy to excite the $^2B_2$ resonance is close this value and we cannot eliminate the possibility that it is physically above the ionization energy. It is possible, therefore, that the parent state of the $^2B_2$ resonance is an autoionizing excited state of neutral H_2O—at least at some geometries.

From the equilibrium geometry of the neutral, the resonance states may be followed adiabatically toward the two-body breakup arrangements in which the electron is attached to one of the fragments or H-OH or O-H_2. We identified the proper asymptotes in these two arrangements previously [25]. In the first of these arrangements, the $^2B_1$ and $^2A_1$ states correlate with H^-+OH ($^2\Pi$), while the $^2B_2$ state correlates with H^-+OH ($^2\Sigma$), leaving the OH fragment excited. In the second, the $^2B_1$ state correlates with ground-state H_2+O^-. The $^2A_1$ state is found at a much higher energy, as H_2(triplet $1\sigma_g 1\sigma_u$)+O^-, and does not have a bound two-body asymptote in this arrangement.

An additional complication is that the $^2B_2$ surface is inherently double-valued. As described in Ref. [25], its lower asymptote is ground-state H_2+O^-, while the upper asymptote of this surface in this arrangement is not electronically bound, and corresponds to O (^1D) plus a resonant state of H_2^-. In our previous study [25], we did not determine which resonant state of H_2^- is involved. The double-valuedness of the $^2B_2$ surface presents a problem for our treatment because we are unable to fully characterize both sheets of this surface for all geometries. We instead define a single surface which interpolates between the two sheets within the three-body breakup region. We will attempt to identify any discrepancies between the results here and the experimental ones which we might ascribe to this omission. However, it is likely that this feature of the adiabatic manifold only plays a significant role for three-body breakup, a channel which we will not consider in paper II.

We do, however, include the $^2A_1$-$^2B_2$ conical intersection in the current treatment, because it is critical for a description of the dynamics of dissociative electron attachment via the $^2B_2$ state. This conical intersection is a consequence of the crossing of the $1b_2$ and $3a_1$ orbital energies as the bond angle is varied, and has analogs in both the singlet and triplet A_1 and B_2 states of the neutral, which exhibit conical intersections near the present one.

The symmetry labels $^2B_1$, $^2A_1$, and $^2B_2$ are appropriate when the H_2O molecule has C_{2v} symmetry, i.e., when the OH bond lengths are equal. When the OH bond lengths are unequal, the molecule belongs to the C_s point group. The appropriate symmetry labels in those geometries are $^2A''$, 1 $^2A'$, and 2 $^2A'$. Due to the conical intersection, the lower (1) and upper (2) $^2A'$ states may each correspond to either $^2A_1$ or $^2B_2$, depending on the bond angle. A complete discussion of the topology of the anion surfaces is given in Ref. [25].

III. FIXED-NUCLEI ELECTRON SCATTERING CALCULATIONS

The resonance positions and widths are extracted from the results of fixed-nuclei scattering calculations carried out at physical (real) energies. The scattering calculations yield an S matrix whose energy dependence is analyzed to determine the location of the resonance pole in the complex energy plane as a function of nuclear geometry. These calculations are fully *ab initio*. We use the complex Kohn variational method [26, 27, 28, 29, 30, 31, 32, 33, 34, 35], which provides a stationary principle for the S matrix. Since detailed descriptions of the method have been given elsewhere [34, 35], we will limit ourselves here to a brief summary to establish the terminology we will use to describe our numerical calculations.

The $(N+1)$-electron scattering wavefunction is represented explicitly in this calculation, using the standard methods of quantum chemistry: one-electron molecular orbitals are assembled as sums of multicenter contracted Cartesian Gaussian functions, products of which define N-electron configuration state functions used to construct the target states. This basis, augmented with additional Gaussian functions and numerical continuum functions to describe the scattered waves, is also used to expand the $(N+1)$-electron wave function.

Thus, key components of this calculation include the

appropriate choice of one-electron orbital and multielectron configuration bases defining the target states and the resonance state. Not only must the resonance state be accurately represented, but also the target states into which it decays. This requirement becomes more difficult with increasing resonance energy, as more target states become energetically accessible as decay channels.

A. Representation of the wavefunction and matrix elements

In our implementation of the complex Kohn variational method, the $(N+1)$-electron scattering wavefunction is expanded as

$$\Psi^{(+)}_{\Gamma_0} = \mathcal{A}\Big[\sum_{\Gamma}\chi_\Gamma(\mathbf{r}_1...\mathbf{r}_N)F^{(+)}_{\Gamma\Gamma_0}(\mathbf{r}_{N+1}) + \sum_{\mu} d^{\Gamma_0}_{\mu}\Theta_\mu(\mathbf{r}_1...\mathbf{r}_{N+1})\Big]. \tag{3}$$

The first sum in Eq. (3) is over target states $\chi_\Gamma(\mathbf{r}_1...\mathbf{r}_N)$ explicitly included in a close-coupling expansion, which may be energetically open or closed. The antisymmetrizer is denoted by $\mathcal{A}$, and the scattered wave associated with channel Γ is further expanded as

$$F^{(+)}_{\Gamma\Gamma_0}(\mathbf{r}) = \sum_i c^{\Gamma\Gamma_0}_i\varphi_i(\mathbf{r}) + \delta_{\Gamma\Gamma_0}\sum_{lm}\Big[J_{lm}(k_\Gamma\mathbf{r})\delta_{ll_0}\delta_{mm_0} + T^{\Gamma\Gamma_0}_{ll_0mm_0}G^{(+)}_{lm}(k_\Gamma,\mathbf{r})\Big]/k_\Gamma^{\frac{1}{2}}r \tag{4}$$

for incoming boundary conditions in the target channel Γ_0 with initial l_0m_0 quantum numbers for the incident electron. The functions $\varphi_i(\mathbf{r})$ in Eq.(4), which we denote as "scattering orbitals", are Gaussian molecular orbitals that are orthogonal to the "target orbitals" used to construct the target states χ_Γ. Thus, one of the first steps in the complex Kohn calculation is the partitioning of the one-electron Hilbert space into the sets of target and scattering orbitals. The functions J_{lm} and $G^{(+)}_{lm}$ in Eq.(4) are constructed from products of radial functions (j_l and $g^{(+)}_l$) times angular functions that are real-valued combinations of spherical harmonics Y_{lm} consistent with the spatial symmetry of the anion. These functions are then Schmidt orthogonalized to the target and scattering molecular orbitals. The function j_l is the regular Ricatti-Bessel function, while $g^{(+)}_l$ is a numerically generated continuum function that is regular at the origin and behaves asymptotically like the outgoing Riccatti-Hankel function:

$$g^{(+)}_{\Gamma lm}(k_\Gamma,r) \underset{r\to\infty}{\longrightarrow} h^{(+)}_l(k_\Gamma r). \tag{5}$$

It is obtained by solving the driven radial equation,

$$\left(k^2_\Gamma - \frac{\partial^2}{\partial r^2} + \frac{l(l+1)}{r^2}\right) g^{(+)}_{\Gamma l}(k_\Gamma,r) = rj_l(k_\Gamma r)\exp(-\alpha r^2), \tag{6}$$

subject to the stated boundary conditions. For all calculations presented here, we use $\alpha = 0.04$.

For energetically closed channels, only the scattering orbitals $\varphi_i(\mathbf{r})$ are included in the sum in Eq.(4); the continuum functions j_{lm} and $g^{(+)}_{\Gamma lm}$ are not included. Thus, the calculation can give S matrices that are discontinuous across channel thresholds. To minimize this problem, we include additional diffuse Gaussian functions in the scattering orbital basis to represent the wavefunction in barely-bound channels. In any case, the resonance energies can be formally discontinuous across channel thresholds; their discontinuities are not due to errors in the calculation, but instead are properties of the true resonance states [37].

The second sum in Eq.(3) is over square-integrable $(N+1)$-electron configurations Θ_μ constructed exclusively from target orbitals. For convenience we refer to the $(N+1)$-electron configurations as the "Q space" and to the close-coupling part of the expansion of the wavefunction as the "P space" of the calculation. The P space may be further divided into the bound component—built from $(N+1)$-electron configurations incorporating only Gaussian orbitals—and the "free" component, corresponding to the target states times continuum functions.

Two approximations are made in calculating the matrix elements of the electronic Hamiltonian with respect to the antisymmetrized basis functions of Eq.(3). The exchange portion of all matrix elements within P space that involve "free" components, as well as the matrix elements between Q space and the free components of P space, are assumed to be zero. These approximations follow from the orthogonalization of the free functions to the bound molecular orbitals and the assumed completeness of the combined sets of target + scattering orbitals over the restricted region of space spanned by the target orbitals. Errors associated with these approximations are minimized by keeping the target orbitals compact and by augmenting the set of scattering orbitals with functions that extend beyond the target orbitals so that the orthogonalized continuum functions are separated from the target orbitals by a large region of space. Further details concerning these approximations can be found in Refs. [34, 35].

B. Target states and basis

The description of a complex Kohn calculation requires the specification of the target states χ_Γ, the Q space configurations Θ_μ, and, for the expansion of the channel eigenfunctions, the scattering orbitals φ_i and the lm pairs included in the asymptotic partial wave expansion. We first turn our attention to the target orbitals and states.

The one-electron orbital basis was constructed entirely from SCF orbitals. We began with the following primitive Gaussian basis. On the oxygen, we used Dunning's triple-ζ basis [39] plus polarization (d) and Rydberg (s, p,

TABLE I: Fifteen lowest H_2O target states for Kohn calculation: energies at the equilibrium geometry r_1=r_2=1.8a_0, $\theta = 104.5°$, and coefficient of dominant configuration in CI expansion, compared to energies from van Harrevelt and van Hemert [38] and from our previous complex Kohn study[22].

State	Energy (hartree)	Excitation energy (eV)			Dominant config.	
	Current	Current	Prev[22]	Ref. [38]	Config.	Coef.
$^1A_1$	-76.0417104	0.0	0.0	0.0		0.9883
$^3B_1$	-75.8042082		6.463		$1b_1 \rightarrow 4a_1$	0.9944
$^1B_1$	-75.7907517	6.829	7.932	7.63	$1b_1 \rightarrow 4a_1$	0.9960
$^3A_2$	-75.7294891	8.496	9.511		$1b_1 \rightarrow 2b_2$	0.9966
$^1A_2$	-75.7268244	8.568	9.611	9.60	$1b_1 \rightarrow 2b_2$	0.9963
$^3A_1$	-75.7196285	8.764	9.926		$3a_1 \rightarrow 4a_1$	0.9588
$^3A_1$	-75.7114283	8.987			$1b_1 \rightarrow 2b_1$	0.9593
$^1A_1$	-75.7100565	9.025	10.534	9.95	$1b_1 \rightarrow 2b_1$	0.7224
$^3B_1$	-75.7072318	9.101			$1b_1 \rightarrow 5a_1$	0.9959
$^1B_1$	-75.7060192	9.134			$1b_1 \rightarrow 5a_1$	0.9946
$^1A_1$	-75.6876243	9.635			$3a_1 \rightarrow 4a_1$	0.7012
$^3B_1$	-75.6863850	9.669			$1b_1 \rightarrow 6a_1$	0.9936
$^1B_1$	-75.6826701	9.770			$1b_1 \rightarrow 6a_1$	0.9951
$^3B_2$	-75.6691870	10.137			$1b_1 \rightarrow 1a_2$	0.9952
$^1B_2$	-75.6688136	10.147			$1b_1 \rightarrow 1a_2$	0.9940

and d) functions, augmented with an s function with exponent 0.0955 and a p function with exponent 0.774. On the hydrogen, we modified the double-ζ plus diffuse basis of Chipman [40]. Chipman's basis consists of four contracted s functions and one p function. The most diffuse s function has exponent 0.0483. We replaced the single p function with two p functions with exponents 0.55 and 0.13, which were chosen to minimize the energy of the H^- anion given by full CI in this basis, which was -0.52190 hartrees, corresponding to a hydrogen electron affinity of 0.59591eV, which recovers most of the experimental value of 0.75419eV. The total size of the contracted target basis was 54.

Using this basis, we first performed a two-shell, generalized SCF calculation corresponding to the average of a ten-electron (neutral H_2O) and nine-electron (cation H_2O^+) SCF calculation. The purpose of such a calculation is to obtain a basis that can describe both the neutral and Feshbach resonance wavefunctions, recalling from the previous section that the Feshbach resonances may be approximately described as two $4a_1$ electrons bound to different states of the cation core. Further details about the generalized SCF calculation can be found in the EPAPS archive[41].

The set of target orbitals used to construct the neutral states χ_Γ included a total of eleven orbitals—the five SCF orbitals plus six of the virtual orbitals: three a_1, labelled $4a_1$ - $6a_1$; the $1a_2$; the $2b_1$; and the $2b_2$. The target states were obtained from a restricted configuration-interaction calculation within this 11-orbital space, in which the $1a_1$ and $2a_1$ orbitals were constrained to be doubly occupied, and all single and double excitations from the $1b_2$, $3a_1$, and $1b_1$ orbitals into the set of six virtual orbitals were included. This "all singles and doubles" calculation is designed to account for the single excitations describing the dominant configurations of the excited states, plus relaxation of the remaining orbitals to first order; it also can describe correlation in the target, particularly in the ground state.

Near the equilibrium geometry of the neutral, this description of the target states puts the excited states slightly lower in energy, relative to the ground state, than appropriate, but otherwise represents key features of their potential-energy surfaces well. In Table I, we list the energies of the low-lying target states at the equilibrium geometry of the neutral, along with the results of van Harrevelt and van Hemert [38].

For the close-coupling expansion of the scattering wavefunctions, we selected sets of target states χ_Γ based on spin and spatial symmetry. At higher energies, a larger number of target states was required to converge the complex Kohn calculation, and therefore we used a different number of target states for calculations on the $^2A''$ ($^2B_1$), the 1 $^2A'$ ($^2A_1$ or $^2B_2$), and the 2 $^2A'$ ($^2B_2$ or $^2A_1$) states. For calculations of the $^2A''$ resonance, we included 15 target states, which near equilibrium geometry are the 15 lowest energy states listed in Table I. For the 1 $^2A'$ state calculation, we added 14 additional states of A' symmetry, for a total of 29 states. For the 2 $^2A'$ calculation, we added an additional eight A'' states, for a total of 37 states. The calculations are all converged with respect to the target state expansion at the equilibrium geometry of the neutral, but there are some geometries at which the calculations are not fully converged.

The $(N+1)$-electron configurations Θ_μ are constructed from the target orbitals and describe correlation, relax-

ation, and the penetration of the incident electron into the target. For the present calculation, they include the dominant configurations which contribute to the resonant states. This set of configurations was again obtained by keeping the $1a_1$ and $2a_1$ orbitals doubly occupied and distributing the other seven electrons over the remaining target orbitals, including at least one but no more than three electrons in the ($4a_1$, $5a_1$, $6a_1$, $1a_2$, $1b_1$, $2b_2$) virtual space.

C. Scattering orbitals and insertion basis

Of the original 54 molecular orbitals, 11 were used for the description of the target and the remaining 43 orbitals were included in the set of scattering orbitals φ_i. To these 43 orbitals we added an additional set of contracted Gaussian functions, all centered on the oxygen. This "insertion basis" is included to improve the two approximations mentioned above associated with the neglect of certain bound-free and free-free matrix elements.

The insertion basis was constructed from even-tempered sets of eight p- and d-type primitive Gaussian functions, η_i. (To avoid linear dependence, we do not include s-type Gaussians separately, but rather include all Cartesian components of the d-type functions.) The exponents started at 0.07 for the p-wave set and 0.075 for the d-wave set, and in both cases the ratio of consecutiveexponents was 0.8. From these sets of primitive functions, we constructed a set of six p and six d-type contracted, orthogonal functions that were designed to have the minimum overlap with the most diffuse functions in the target basis. To this end, we constructed a matrix representation, in the primitive insertion basis, of the operator P which projects onto the space spanned by the most diffuse functions included in the target basis, i.e.,

$$P_{ij} = \sum_k \langle \eta_i | \phi_k \rangle \langle \phi_k | \eta_j \rangle, \tag{7}$$

where the ϕ_k are the most diffuse functions of the target basis, Schmidt-orthogonalized. These functions comprised the two s- , two p- and one d-type target functions with the smallest exponents.

Diagonalization of P gave two p- and two d-type vectors with eigenvalues close to unity, which were discarded. The other six p- and six d-type functions Ψ_n were retained as the insertion basis, giving a total of 6 × (3+6) = 54 additional Cartesian Gaussian functions and a total (target plus augmented scattering) set of 108 functions. The exponents and contraction coefficients of the insertion basis are listed in the EPAPS archive[41].

We should remark that the insertion basis we use is very similar to the exterior basis used by Nestmann and others [42] for use in R-matrix calculations. In the R-matrix method, the Gaussian basis must represent the outgoing wave within the finite R-matrix box. Nestmann's basis is designed for a 20-bohr box and represents the continuum functions well for energies up to about 12 eV. In the current work, the exponents were chosen to provide as complete a basis as possible within approximately 20 atomic units from the oxygen center.

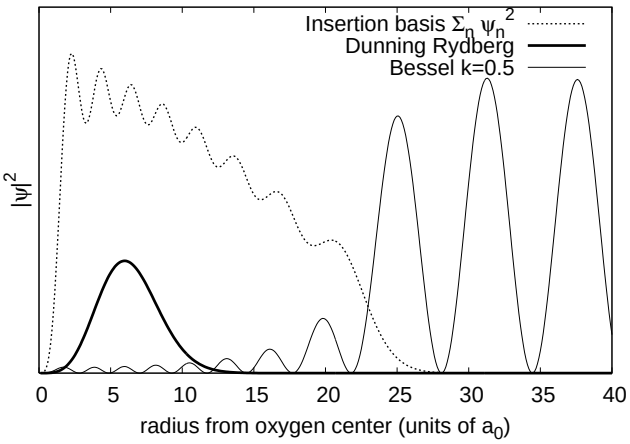

FIG. 2: Modulus squared of diffuse basis functions for l=1 (p waves) used in the Kohn calculations, centered on oxygen nucleus: sum of insertion basis (dashed line), Rydberg p-function with exponent 0.028 (thick solid line), and orthogonalized Bessel function $j_1(kr)$ (thin solid line). The Bessel function has k=0.5a_0^{-1} and arbitrary normalization. See text for further explanation.

A pictorial representation of the basis set used in the Kohn calculations, which demonstrates the extent of the diffuse target, insertion, and continuum basis functions, is shown in Fig. 2. In this figure, the squared modulus of various members of the diffuse and continuum basis for l=1 (p waves) is plotted with respect to the radial distance from the oxygen nucleus. The most diffuse basis function used in the target calculations, with exponent 0.028, is plotted along with the sum of the squared moduli of the insertion basis, $\sum_n \Psi_n^2$, and that of the l=1 Bessel function, orthogonalized to the insertion basis.

D. Extracting resonance parameters

The complex Kohn calculation was performed at 10 to 20 energies around the resonance location, and the S matrices produced were fitted to a Breit-Wigner form,

$$S_{nlm,n'l'm'}(E) = S^{bg}_{nlm,n'l'm'}(E) + \frac{\gamma_{nlm}\gamma_{n'l'm'}}{E - E_R + i\frac{\Gamma}{2}}, \tag{8}$$

where the background S^{bg} is either linear or quadratic in E, to obtain the resonance energy E_R and the width Γ at each geometry, as well as the partial amplitudes γ_{nlm}, labeled by the decay channel index nlm, where n is electronic target state and lm label the angular momentum of the emitted electron. The modulus squared of the partial amplitudes corresponds to partial widths, and in particular, the partial width with respect to decay

into the electronic channel n is

$$\Gamma_n = \sum_{lm} |\gamma_{nlm}|^2 . \quad (9)$$

Unitarity of the S matrix implies $\sum_n \Gamma_n = \Gamma$.

Dissociative electron attachment to water occurs at incident electron energies sufficient to excite multiple states of the neutral H_2O target. The definition of the resonance location and width in terms of the pole in the S matrix, as per Eq.(8), poses a problem near target state thresholds. In our Born-Oppenheimer treatment of this process, we examine the behavior of the fixed-nuclei resonance width and location as the nuclear geometry is varied. At some nuclear geometries, the resonance location may cross an excited state threshold.

According to analytic S matrix theory as described by Newton [37], in such a situation it is generally not the same pole of the S matrix that is responsible for the resonance feature in the cross section both above and below a channel threshold. In such a case, in accordance with the formal theory, we observe that one pole quickly replaces another as the geometry is varied, so that the location of the pole identified with the resonance is effectively discontinuous near such a threshold. In contrast, the description of dissociative electron attachment under the Local Complex Potential model[1, 2, 3, 4, 5] requires continuous potential-energy surfaces. As a result, we construct a global representation of the resonance width that smoothly interpolates through such discontinuities.

IV. RESULTS OF SCATTERING CALCULATIONS

At the equilibrium geometry of the neutral, the resonance positions of the $^2B_1$, $^2A_1$, and $^2B_2$ states were calculated to be 6.09, 8.41, and 11.97 eV, respectively, with widths of 10.31, 28.8, and 193 meV and partial widths with respect to decay to the ground state of 10.31, 10.30, and 9.135 meV. At equilibrium target geometry, each resonance lies below its parent state. The $^2B_1$ lies 370 meV below its $^3B_1$ parent. The $^2A_1$ lies 351 meV below its triplet parent, which in turn is only 223 meV below the next $^3A_1$ state ($1b_1^{-1}\ 2b_1^1$). (These two $^3A_1$ states are in fact on the edge of an avoided crossing, at the equilibrium geometry of the neutral, and thus the binding energy of the A_1 resonance versus its parent is slightly reduced by this avoided crossing.) The $^2B_2$ lies 1.831 eV above the first $^3B_2$ state, which has a dominant configuration $3a_1^{-1}2b_2^1$, and 471 meV below its triplet $1b_2^{-1}4a_1^1$ parent. The latter state is the 26th root of the target CI, and has a vertical energy of 12.438eV; this value is near the ionization potential of water, 12.621eV, which calls into question whether the $^3B_2$ parent is a true bound electronic state of the target at all, at the equilibrium geometry of the neutral. If not, it is likely that it exists instead as a low-lying Feshbach resonance in e^-+H_2O^+ Coulomb scattering.

We performed scattering calculations along 13 distinct one-dimensional cuts within nuclear configuration space. A dense set of points was chosen along each of these cuts to give an accurate and descriptive picture of the behavior of the resonances. The upper 2 $^2A'$ resonance was examined along nine of the 13 cuts. Six of the 13 total cuts lie in C_{2v} geometry: symmetric stretch ($r_1 = r_2$) for θ_{HOH}=75°, 105°, and 150°; bend for r_1=r_2=1.81a_0 and 2.41a_0; and versus the Jacobi coordinate R for constant HH bond length r_{HH}=1.40a_0. The remaining cuts are bend at r_1=1.81, r_1=2.41a_0, and single-bond stretch at the six combinations of r_1={ 1.81, 2.41a_0 } and θ_{HOH}={ 75, 105, 150° }. For the 2 $^2A'$ surface we did not calculate the three cuts at 150°, nor the bending cut at (r_1=1.81, r_2=2.41).

We present results for the three cuts which pass through the equilibrium geometry of the neutral: as a function of bending angle θ for r_1=r_2=1.81a_0; as a function of r_2 for r_1=1.81a_0 and θ=105°; and as a function of the equal bond lengths for symmetric stretch at θ=105°. Also we present data for the cut in Jacobi coordinates at r_{HH}=1.4a_0, C_{2v} symmetry (γ=π/2), which does not intersect the target equilibrium geometry.

These calculations test the limits of our implementation of the complex Kohn method, and therefore it is useful to have a measure of the performance of the calculation. One such measure is the modulus of the S matrices produced. The physical S matrix is unitary, with eigenphases having modulus 1. At the equilibrium geometry of the neutral, at the center of the $^2B_1$ resonance, the modulus of the most nonunitary calculated S matrix eigenphase was 1.005.

The $^2A_1$ calculation performed even better, yielding a value of 1.004 for the modulus of most nonunitary eigenphase. The corresponding value for the $^2B_2$ calculation, at higher energy with 24 open electronic states of the target and a 46×46 S matrix, was 1.2. When in C_s symmetry the on-resonance $^2B_2$ calculation obtains a largest size of 120×120 channels at r_1=1.61a_0, r_2=1.81a_0, θ_{HOH}=105°, at which point the S matrix is also significantly nonunitary. We note in passing that in all cases, the unitarity of the calculation is much improved for energies off-resonance.

A. Bend, $r_1 = r_2 = 1.81a_0$

Plots of the resonance positions and target states energies included in the Kohn calculation for this cut are shown in Fig. 3. The resonance energies are lines, and the target energies are connected dots. The large-dotted lines are those target states included in all calculations; the small-dotted lines are not included in the $^2B_1$ calculation (small dotted A' states) or not included in both the $^2B_1$ and 1 $^2A'$ calculation (small dotted A" states). Dots are filled for A_1 and A_2 symmetries, and open for B_1 and B_2 symmetries.

Within this cut, the target state curves compare well

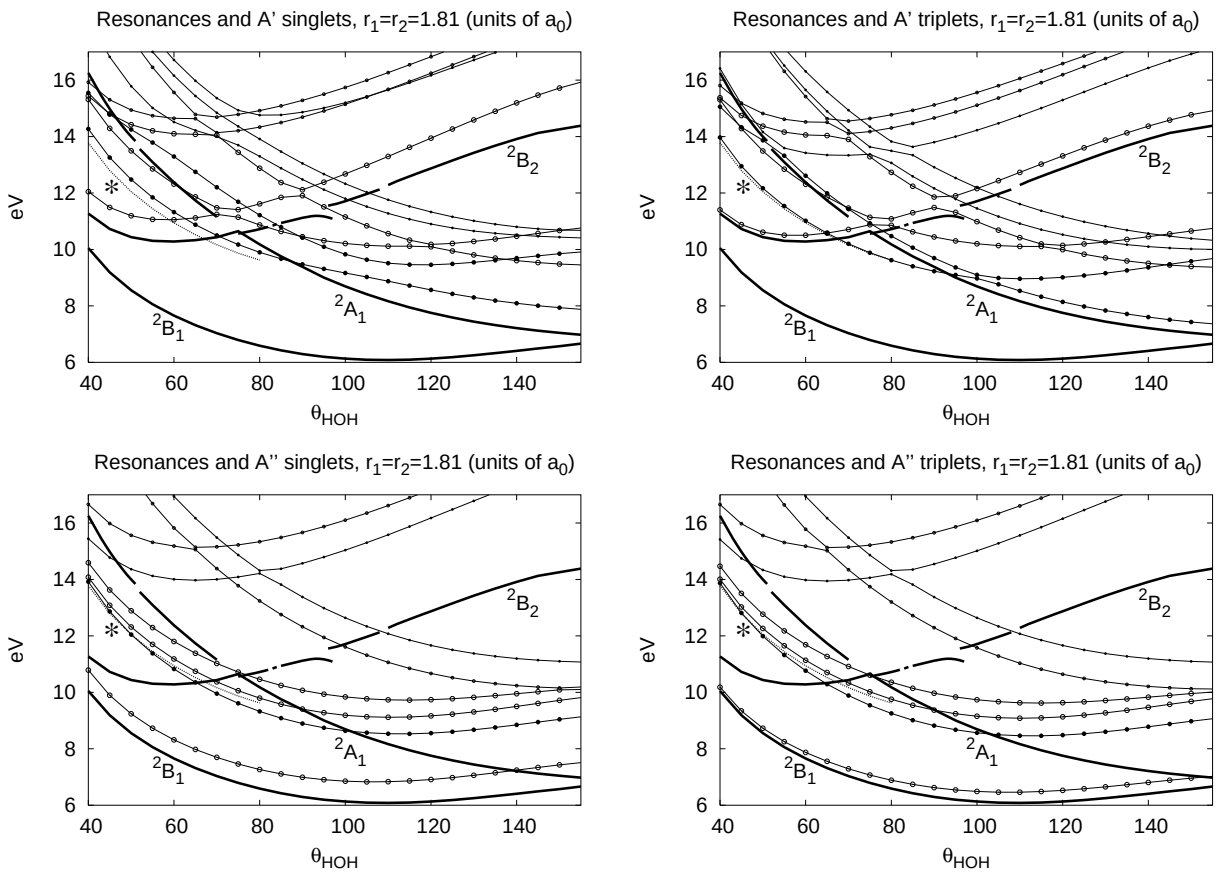

FIG. 3: Location of resonances (solid curves) and target states (dotted curves) at r_1=r_2=1.81 (units of a_0), as function of bending angle θ_{HOH}. Filled dots, A_1 and A_2 target states; empty dots, B_1 and B_2 target states. The dotted curves, marked by an asterisk, refer to a second $^2A_1$ resonance discussed in the text.

with the high-quality CI results of Harrevelt and van Hemert[38]. As previously mentioned and shown in Table I, at the equilibrium geometry of the neutral the Kohn target states are about 1eV below their proper location. However, aside from this shift, the shapes of these bending potentials are quite comperable to those of Ref. [38]. The 1 $^1B_1$ curves from both calculations are quite similar. Both calculations show an avoided crossing between the 2 $^1A_1$ and 3 $^1A_1$ states (near $\theta_{HOH} = 105°$ in our calculations), where they change character between $1b_1^{-1}2b_1^1$ and $3a_1^{-1}4a_1^1$, although the crossing is broader in our calculations. The 1 $^1B_2$ state undergoes several changes in character as it passes several avoided crossings, but it seems that the Kohn target curve is again simply shifted by about 1eV lower versus the results of Ref [38]. The 1 $^1B_2$ state is predominantly $3a_1^{-1}2b_2^1$ at $\theta_{HOH} = 180°$ and changes character to $1b_1^{-1}2a_2^1$ at the sharp avoided crossing near 120°. The 1 $^1A_2$ state nearly parallels the 1 $^1B_1$ state, slightly less than 2eV above it, for both calculations.

Along the cut shown in Fig. 3, the $^2B_1$ Feshbach resonance stays below its $^3B_1$ parent, except at very small bending angles θ_{HOH}, and therefore is below all target states except the ground electronic state. The $^2A_1$ state follows its triplet parent, $^3A_1$ [H_2O]$3a_1^{-1}4a_1^1$ configuration. At most angles this configuration describes well one

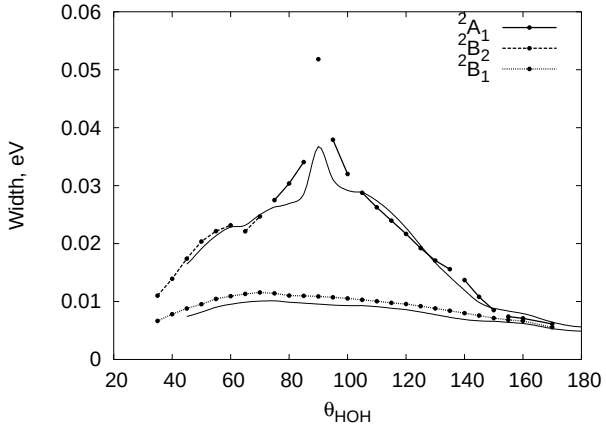

FIG. 4: Width of the $^2B_1$ and 1 $^2A'$ resonances (dots) with respect to bending angle θ for r_1=r_2=1.81 (units of a_0), with interpolated global representation (plain lines).

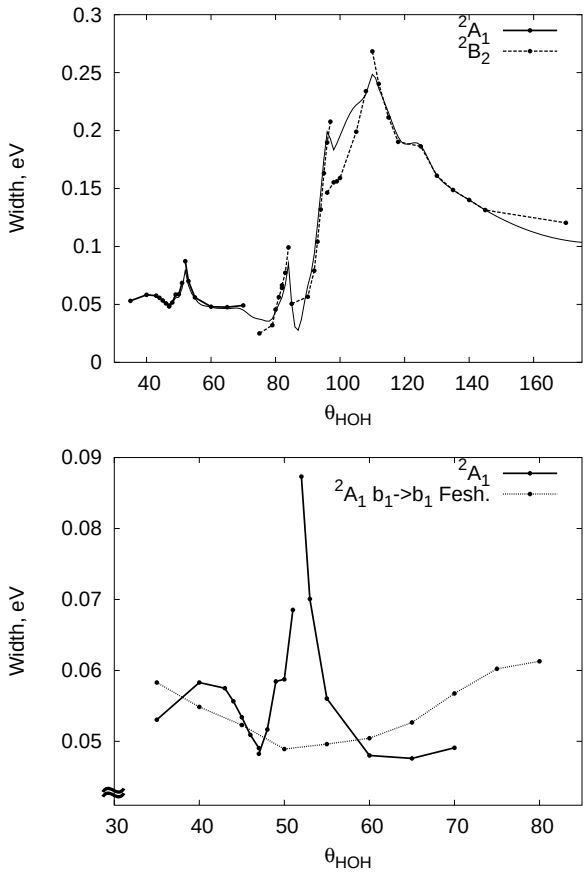

FIG. 5: Top, width of the 2 $^2A'$ resonance (dots) with respect to bending angle θ for r_1=r_2=1.81 (units of a_0), with interpolated global representation (plain line). Bottom, zoom of width in $^2A_1$ symmetry, with width of novel $^2A_1$ ($[H_2O]1b_1^{-1}2b_1^14a_1^1$) Feshbach resonance.

of the target states, except where there are avoided crossings. There are two avoided crossings involving this state: the one with the $[H_2O]1b_1^{-1}2b_1^1$, around θ_{HOH}=100° and 9.5eV, and also one with the $[H_2O]1b_2^{-1}2b_2^1$ state near θ_{HOH}=55° and 13.5eV. Near both of these crossings, there are discontinuities as the resonances cross the avoided state threshold. For the former avoided crossing, the discontinuity in the resonance position is not visible on the scale plotted in Fig. 3, but there is a significant discontinuity in the $^2A_1$ width at θ_{HOH}=95°; for the latter crossing, the discontinuity in position near θ_{HOH}=50° is apparent as well. The $^2B_2$ resonance also follows its triplet parent configuration and parent state through avoided crossings with the $[H_2O]1a_1^{-1}2b_2^1$ state (avoided crossing at θ_{HOH}=92°; discontinuity at θ_{HOH}=96°) and $[H_2O]1b_1^{-1}1a_2^1$ state (avoided crossing at θ_{HOH}=79°; small discontinuity at θ_{HOH}=83°). The former discontinuity is quite large ($\sim$ 0.25eV).

The widths for the $^2B_1$ and 1 $^2A'$ ($^2B_2$ or $^2A_1$) states along this cut are shown in Fig. 4. Both the raw Kohn results (dotted lines) and an interpolated version (plain lines, defined later, in Sec. IV E) are plotted. The width of the $^2B_1$ state is relatively constant. The $^2A_1$ state attains a relatively large width around θ=95° as it crosses multiple target states, but then the width decreases before the $^2A_1$ state intersects the $^2B_2$ state between θ_{HOH}=70 and 75°. At this geometry the widths of the $^2A_1$ and $^2B_2$ Feshbach resonances happen to be nearly equal, and so there is only a small discontinuity as the 1 $^2A'$ resonance changes symmetry from $^2A_1$ to $^2B_2$ as the bond angle is decreased. In Fig. 4 adjacent data points are connected by line segments only if no target states are crossed as the geometry is varied between them. Therefore one can see that at most crossings on the 1 $^2A'$ surface the discontinuity in the resonance energy is in fact small.

The width of the 2 $^2A'$ ($^2A_1$ or $^2B_2$) resonance is plotted in Fig. 5. The $^2B_2$ state attains a large width (0.25eV, τ=2.5fs) as it becomes the 2 $^2A'$ resonance, and in particular as it rises above the B_2 target states near θ_{HOH}=82° and 95°, at which points there are significant discontinuities in the location of the physical resonance pole. In particular, at 95° there is a large discontinuity in the real part of the resonance location: the real parts of the energies of the two poles avoid each other by approximately 0.3eV, whereas the widths avoid by only 0.025eV. In Fig. 5 adjacent data points have been connected if the resonance does not cross a target state of the same spatial symmetry, or otherwise exhibit a large discontinuity. For the $^2B_2$ Feshbach resonance, there are large discontinuities for non-B_2 crossings at the 2 $^1A_1$ crossing near θ_{HOH}=84°, and at the crossing of both the 5 $^3B_1$ and 5 $^1B_1$ near θ_{HOH}=108°.

The calculation supports a different Feshbach resonance of $^2A_1$ symmetry for $\theta_{HOH} < 80°$ along this cut, whose parent is the $[H_2O]1b_1^{-1}2b_1^1$ $^3A_1$ target state, and which would have the dominant configuration $[H_2O]1b_1^{-1}2b_1^14a_1^1$. The location of this Feshbach resonance is also plotted in Fig. 3. For these geometries it is impossible to say whether this is an artifact of the calculation or a physical state, since along this cut, this Feshbach resonance is extremely narrow and is not bound by more than 25meV. A small upward perturbation of the calculated resonance location would lead to its disappearance above its parent. This state is only present when the $[H_2O]1b_1^{-1}2b_1^1$ configuration is the lowest-energy $^3A_1$ target configuration, for then it cannot decay to the triplet or singlet B_1 ($[H_2O]1b_1^{-1}4a_1^1$) target states. This is the case when the bond lengths are modest and the bond angle is small. The Jacobi coordinate cut, which we present in Sec. IV D, gives a better view of the interaction between this Feshbach resonance and the other $^2A_1$ resonance and demonstrates that in fact this $[H_2O]1b_1^{-1}2b_1^14a_1^1$ Feshbach resonance may exist as an asymptote of the $[H_2O]3a_1^{-1}4a_1^2$ Feshbach resonance, due to branching of the adiabatic PES.

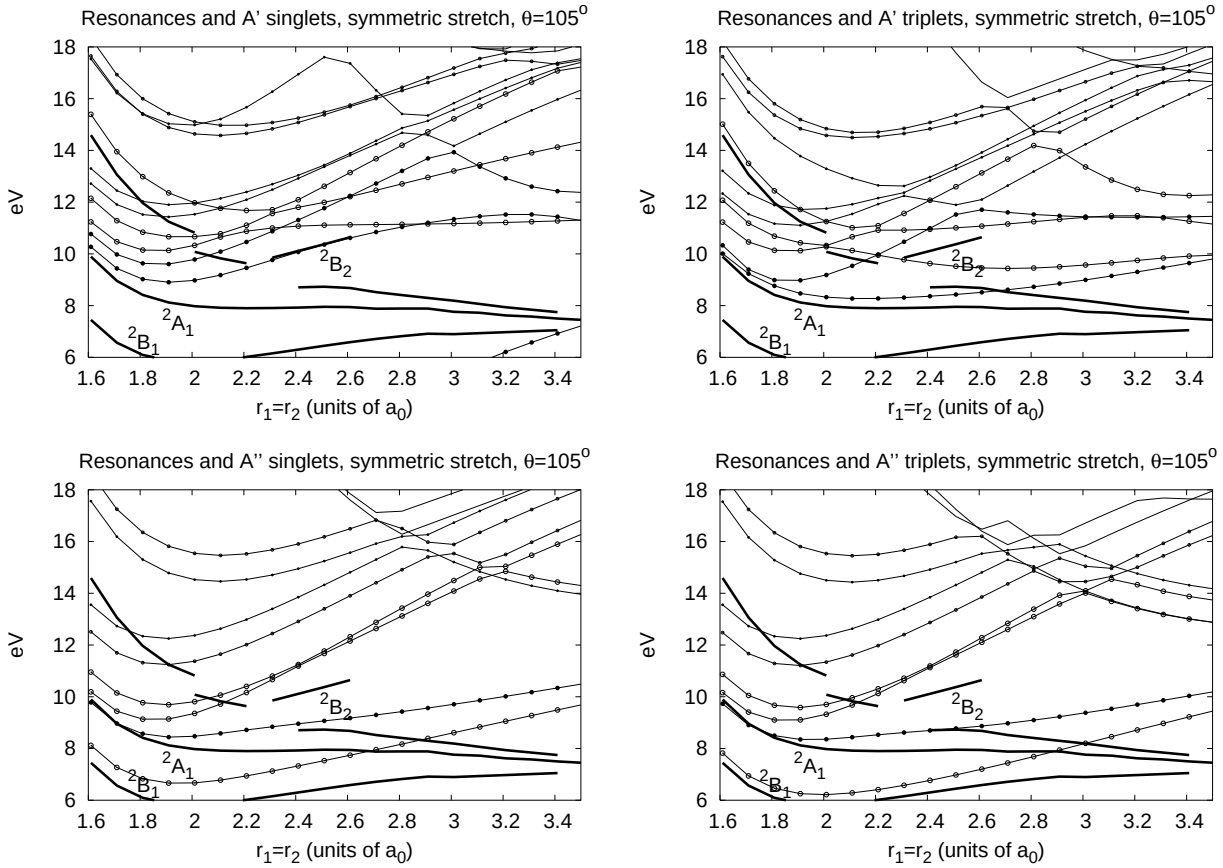

FIG. 6: Location of resonances (solid curves) and target states (dotted curves) at θ=105°, as function of symmetric stretch r_1=r_2. Filled dots, A_1 and A_2 target states; empty dots, B_1 and B_2.

B. Symmetric stretch, $\mathbf{r_1 = r_2}, \theta = \mathbf{105}^\circ$

The target energies and resonance positions along this cut are shown in Fig. 6, with the same conventions as Fig. 3. The (undotted) curves near the top right part of each panel correspond to the first target state of each symmetry that is not included in any of the Kohn calculations. The 1 $^1B_1$ curve is very similar to that of Ref. [38], except that the minimum is at $1.95a_0$, not $2.1a_0$. The 1 $^1A_2$ asymptote of the Kohn target curve is too high by ∼1 eV. The 2 $^1A_1$ and 1 $^1B_2$ state curves are similar to those of Ref. [38], but shifted down ∼0.75 eV, and in fact duplicate the apparent change of character of the 1 $^1B_2$ state at about r_1=r_2=$2.1a_0$.

As the symmetric stretch coordinate r_1=r_2 is increased from the equilibrium geometry at $1.81a_0$, the $^2B_1$ and $^2A_1$ (1 $^2A'$) resonances approach the bound O+H+H$^-$ asymptote of the three-body system and both become bound at approximately r_1=r_2=$3.5a_0$. The $^2B_2$ (2 $^2A'$) resonance exhibits large discontinuities, due to both target state crossings and the interaction with the $^2B_2$ shape resonance as discussed in Ref. [25]. At r_1=r_2>$2.4a_0$, the lower-energy branch of the $^2B_2$ shape-Feshbach system is uncovered beneath the 1 $^3A_2$ state of the target, which correlates to O+H+H.

The widths for these cuts are shown in Figs. 7 and 8, with the same conventions as in Figs. 4 and 5. For

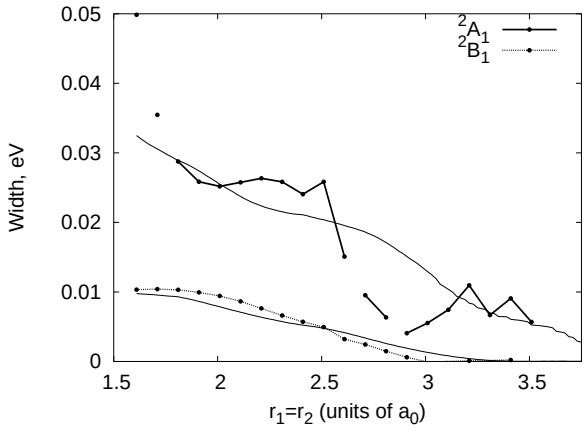

FIG. 7: Width of the $^2B_1$ and $^2A_1$ (1 $^2A'$) resonances (dots) with respect to symmetric stretch r_1=r_2, at θ=105°, with interpolated global representation (plain line).

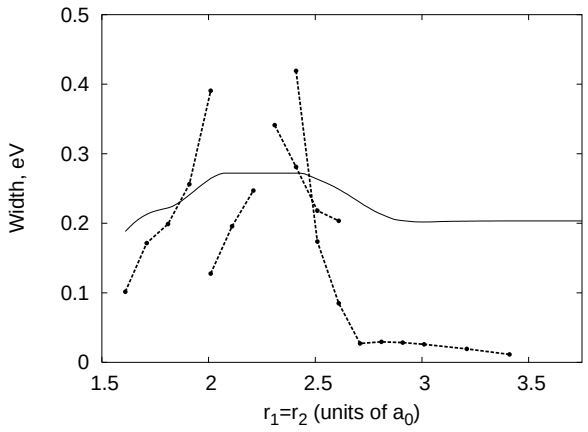

FIG. 8: Width of the $^2B_2$ (2 $^2A'$) resonance (dots) with respect to symmetric stretch, r_1=r_2, at θ=105°, with interpolated global representation (plain line).

the 2 $^2A'$ state, the final branch of the $^2B_2$ state was not included in the global fit, and thus the interpolated value levels off near 0.2eV, corresponding to the width of the penultimate branch at r_1=r_2=2.6 a_0.

C. Single bond stretch, $\mathbf{r_1 = 1.81a_0}, \theta = \mathbf{105}^\circ$

The resonance locations and Kohn target state energies along this cut are shown in Fig. 9. Along this cut towards increasing r_2, the 1 $^3A''$, 1 $^1A''$, and 1 $^3A'$ Kohn target states, which correspond to the 1 $^3B_1$, 1 $^1B_1$, and 1 $^3A_1$ states at the equilibrium geometry of the neutral, move downward in energy as they approach the ground-state H+OH asymptote of the fragments. The 2 $^1A'$ (2 $^1A_1$) state surface is repelled by the ground state and is essentially constant, starting at 9 eV, with a gentle maximum at 9.25 eV at r_2=2.5a_0, and approaching 8 eV at the OH($^2\Sigma$)+H asymptote. The difference between this asymptote and the OH($^2\Pi$)+H ground state of the fragments is 4eV for the Kohn states; this may be compared with an earlier calculated value [43] of 5.27eV at r_1=1.80a_0. The results for the excited state singlets are consistently ∼1eV below the results of Ref. [38]. Thus, the ground X $^1A_1$ Kohn target state curve dissociation energy is underestimated by about 1eV along this cut.

Moving towards increasing r_2 along this cut, the $^2A''$ and 1 $^2A'$ Feshbach resonances fall in energy and become bound as H^-+OH(X $^2\Pi$) near r_2=4.5a_0. The 2 $^2A'$ state correlates to the H^-+OH(Σ) asymptote, which lies above the ground state of the neutral, H+OH(X $^2\Pi$); its width therefore goes to zero only asymptotically. The 2 $^2A'$ state has two large discontinuities along this cut. The first, near r_2=2.15a_0, is associated with an avoided crossing between the $^3A'$ parent state and another state that becomes the new parent, correlating to OH($^2\Sigma$)+H, triplet coupled. As r_2 is increased further, the binding energy of the Feshbach resonance with respect to this state decreases to zero at r_2=3.0a_0, and it disappears for r_2>3.0a_0, but by this time a distinct resonance pole which follows the corresponding singlet state [correlating to OH($^2\Sigma$)+H, singlet coupled] has already appeared to take its place.

Along this cut, the binding energies of the Feshbach resonances (which are plotted in the EPAPS archive) with respect to their parents all reach a minimum around r_2=3.25a_0. This is also the geometry at which the middle 2 $^2A'$ branch disappears. It is interesting that this is the case not only for the electronically similar $^2A''$ ($^2B_1$) and 1 $^2A'$ ($^2A_1$) states but also for the final branch of the 2 $^2A'$ state. In each case this minimum is approximately 50meV, which for the 1 and 2 $^2A'$ states is only twice their width, $\Gamma \approx$ 25meV. We certainly cannot be confident that our treatment of the N- and $(N+1)$- electron systems is balanced at the 50meV level. This value is an order of magnitude smaller than the binding energies at the equilibrium geometry of the neutral, and calls into question whether the physical states in fact may rise above their parents near r_2=3.25a_0.

The widths for these cuts are shown in Figs. 10 and 11, with the same conventions as in Figs. 4 and 5. The width of the $^2A''$ state goes smoothly to zero as the resonance becomes bound. In contrast, the 1 $^2A'$ state achieves a large width as r_2 increases, as high as 0.18eV at r_2=4.55a_0. It may do so because it is connected to the ground state by an s-wave matrix element; we suspect that it does do so because at intermediate geometries, the electronic structure is highly correlated, and the orbital description of the resonance is likely to be different from that of the target states, muddling the distinction between Feshbach and shape resonances. In other words, as the 1 $^2A'$ Feshbach resonance dissociates it takes on an increasing degree of shape resonance character, leading to an increase in width. We discuss this issue further in paper II.

D. Jacobi coordinates, $\mathbf{r_{HH} = 1.4a_0}, \gamma = \mathbf{90}^\circ$

One may define a Jacobi coordinate system for H_2O in which r_{HH} is the H−H bond length, R is the distance between the oxygen and the H_2 center of mass, and γ is the angle between the two corresponding vectors. Here we present data along the cut r_{HH}=1.40a_0, γ=90° (C_{2v} geometry), plotted as a function of R. This cut traces the resonances from a squeezed geometry (small θ_{HOH}) towards the O+H_2 arrangement in C_{2v} symmetry. It is uninteresting except for the interaction between the $^2A_1$ (2 $^2A'$) Feshbach resonance with configuration $[H_2O]3a_1^{-1}4a_1^2$ and the second $^2A_1$ Feshbach resonance mentioned above, with configuration $[H_2O]1b_1^{-1}2b_1^14a_1^1$.

In Fig. 12, we show complex Kohn S matrix elements and fitted resonance locations along this cut. This figure requires some explanation. The target state energies are plotted as dots, and the resonance location is plotted as a single, thick solid line. At 15 of the plotted values of R

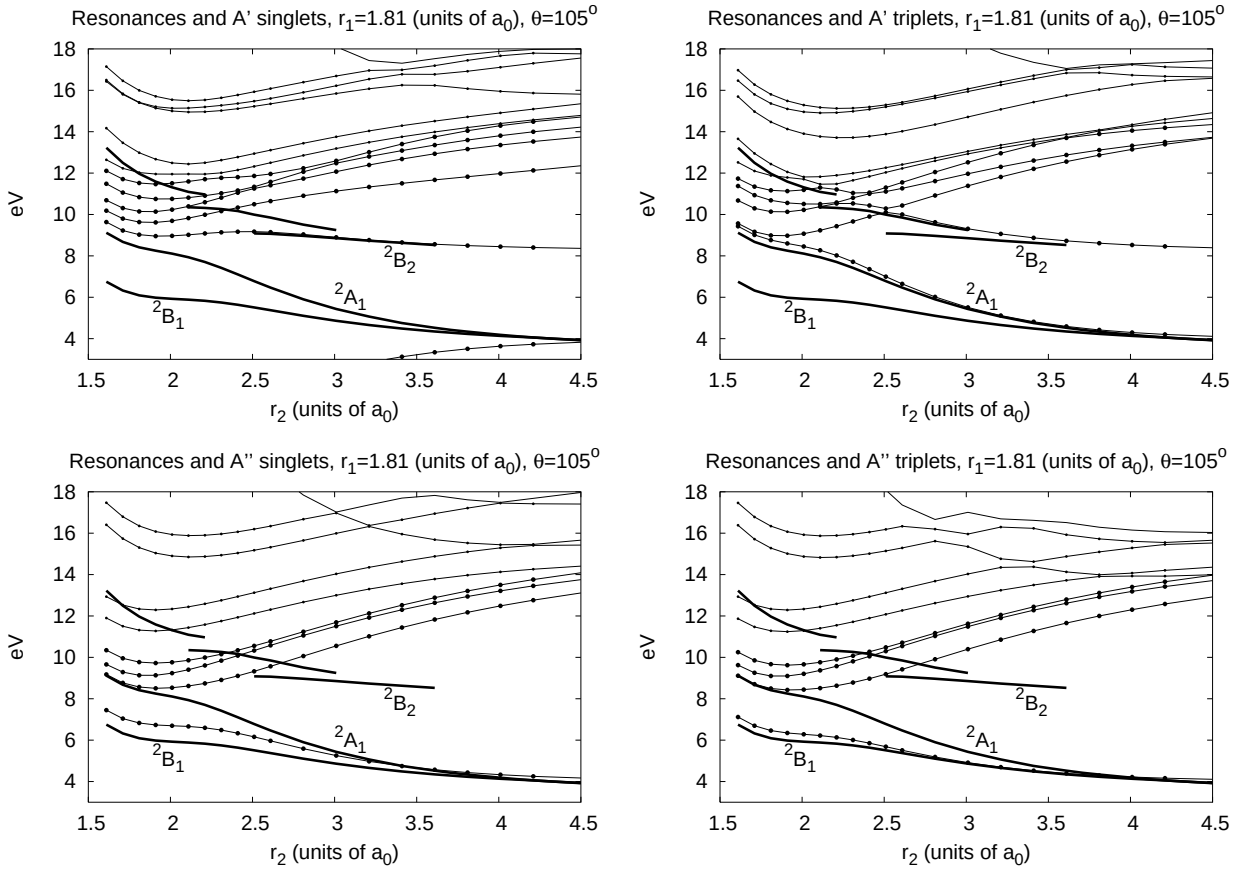

FIG. 9: Location of resonances (solid curves) and target states (dotted curves) at r_1=1.81a_0, θ=105°, as function of r_2.

we have also plotted the real part of the $s \rightarrow s$ S matrix element calculated using the complex Kohn method but with ordinate and abscissa reversed. The scale and origin in the horizontal (ordinate) direction is arbitrary for these S matrix elements.

The leftmost data in this figure are calculated at R=1.67a_0, a geometry that in bond-angle coordinates is approximately (r_1=r_2=1.81a_0, θ_{HOH}=45°). At this geometry, both the [H_2O]$3a_1^{-1}4a_1^2$ Feshbach resonance, at

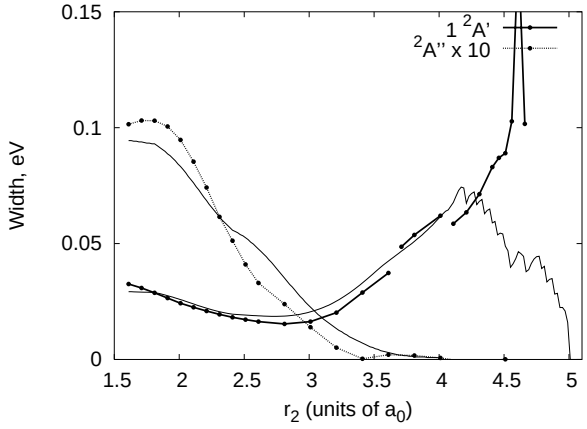

FIG. 10: Width of the $^2A''$ ($^2B_1$) (× 10) and 1 $^2A'$ resonances (dots) with respect to r_2 for r_1=1.81a_0, θ=105°, with interpolated global representation (plain line).

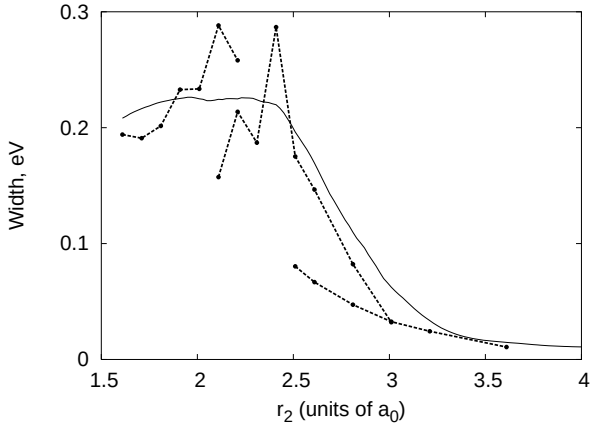

FIG. 11: Width of the 2 $^2A'$ resonance (dots) with respect to r_2 for r_1=1.81a_0, θ=105°, with interpolated global representation (plain line).

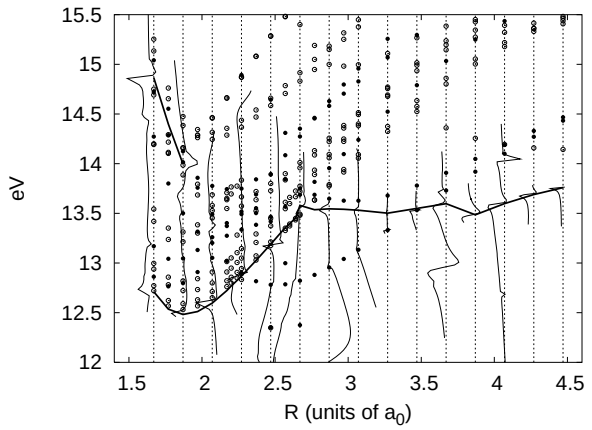

FIG. 12: Location of $^2A_1$ resonances and raw complex Kohn data at r_{HH}=1.4a_0, C_{2v} symmetry (γ=90°) as functions of Jacobi coordinate R. Solid thick line: resonance location. Filled dots: A_1 target states. Empty dots: other target states. Thin lines: real part of $s \rightarrow s$ S matrix element, on an arbitrary scale, as a function of energy at various R, plotted with ordinate and abscissa reversed.

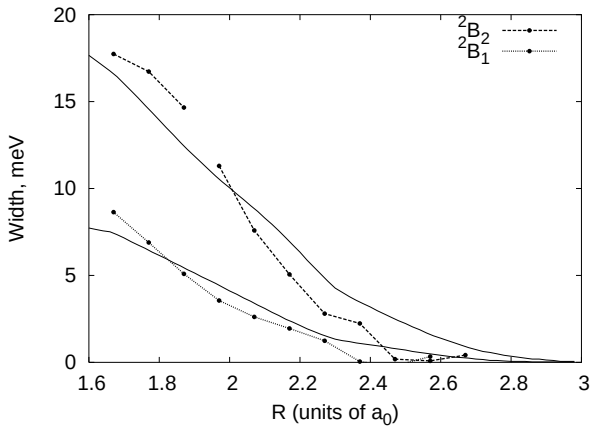

FIG. 13: Width of the $^2B_1$ and $^2B_2$ (1 $^2A'$) resonances (dots) in C_{2v} symmetry with respect to the Jacobi coordinate R for r_{HH}=1.4a_0, with interpolated global representation (plain line).

~14.9eV, and the $[H_2O]1b_1^{-1}2b_1^14a_1^1$ Feshbach resonance, at ~12.75eV, are present and their Breit-Wigner profiles may be seen in the behavior of the S matrix element. As the coordinate R is increased beyond 1.87a_0, however, the main $[H_2O]3a_1^{-1}4a_1^2$ resonance is lost within a web of avoided and actual target state crossings around 14eV. The lower $[H_2O]1b_1^{-1}2b_1^14a_1^1$ Feshbach resonance is still present, however, and is bound by 0.5eV with respect to its $[H_2O]1b_1^{-1}2b_1^1$ $^3A_1$ parent state at R=1.97a_0. This large binding energy brings up the possiblity that this resonance is in fact physical, at least at this geometry, and not simply an artifact of the calculation supported by recorrelation of the target. This Feshbach resonance follows the energy of its $^3A_1$ parent through an avoided crossing near 2.1a_0 and through actual crossings with two $^1A_1$ states at approximately 2.45 and 2.55a_0.

At approximately R=2.67a_0 there is an actual crossing between the $^3A_1$ parent and the $^1A_1$ state, which is a parent of the familiar $[H_2O]3a_1^{-1}4a_1^2$ Feshbach resonance, and at this point, the $[H_2O]1b_1^{-1}2b_1^14a_1^1$ resonance appears to change character to that of the more familiar resonance, as there is a kink in the resonance trajectory and the resonance pole then follows the $^1A_1$ parent as it dissociates toward H_2 ($1\sigma_g1\sigma_u$) + O (^{3}P).

Thus, it appears that the $^2A_1$ Feshbach resonance may undergo an interaction with a different Feshbach resonance of a sort similar to that which occurs [25] within the B_2 manifold between the $[H_2O]1b_2^{-1}4a_1^22B_2$ Feshbach resonance and a $^2B_2$ shape resonance. The difference would be that in the current case, the topology is supported by the disappearance and appearance of different branches of the adiabatic manifold due to the crossing of N-electron target states, whereas in the $^2B_2$ case, it is supported by the underlying $(N+1)$-electron Hamiltonian. Another difference is that the topological complications that may occur on the $^2A_1$ potential-energy surface seem to do so at geometries not sampled by the propagating DEA wavepacket, making them irrelevant to the physical problem, although we did not attempt a comprehensive analysis of this issue. Along this cut, the $^2B_1$ and $^2B_2$ (1 $^2A'$) states quickly become bound as O^-+H_2, and we present the widths of these states in Fig. 13.

E. Global representation of the widths

For the purpose of performing nuclear dynamics calculations, a global representation of the width Γ is required. Global representations were constructed separately for the $^2A''$, 1 $^2A'$, and 2 $^2A'$ states.

The first step in constructing each of these global representations was to define a continuous representation along each of the 13 one-dimensional cuts listed above, which was obtained via cubic splines in the coordinates r_1, r_2, and $\cos(\theta_{HOH})$. Along these lines but beyond the last data points of the cuts in the r_1, r_2, or symmetric stretch directions, the width was either set to the terminal value, or to zero in the case of the large-r region for the asymptotically bound 1 $^2A'$ or $^2B_1$ resonances.

The global representation of the fit was obtained as follows. Each one-dimensional cut is represented by a curve in the three dimensional space of coordinates $\vec{q} = (r_1, r_2, \theta)$. For a desired geometry $\vec{q_0}$, we first calculate for each cut (by interpolation, as explained above) the width at the point which is closest to $\vec{q_0}$. We then take an average of the values at these 13 points, each inversely weighted according to its distance from $\vec{q_0}$. Examples of the interpolated witdh surfaces are shown in the EPAPS archive[41].

V. CI CALCULATIONS FOR THE REAL PART OF RESONANCE SURFACES AND THE NEUTRAL SURFACE

We construct the real part of the resonance energy E_R as a function of the internal nuclear geometry of H_2O using bound-state configuration-interaction calculations. Our task in doing so is to accurately reproduce real-valued component of the physical potential-energy surfaces, taking into account the numerous features of these surfaces which were described in Ref. [25], and, in particular, the conical intersection between the $^2B_2$ and $^2A_1$ surfaces, for which we require a diabatization.

The main configuration-interaction calculations on the resonance states and the ground state of the neutral described below in Secs. V B and V D reproduce the vertical transition energies and all but one of the two-body breakup asymptotes correctly. However, the three-body asymptotes of the main configuration-interaction calculation are all too high in energy (by as much as more than 1eV), and the asymptote of the diabatic $^2A_1$ state is far below its proper $O^-+H_2(\sigma_g^1\sigma_u^1)$ $^3\Sigma_u$ asymptote, instead being degenerate with the other resonances as $O^-+H_2(\sigma_g^2)$. For this reason, we must patch the *ab initio* surfaces produced from the main CI calculation.

We construct global representations of the adiabatic $^2B_1$ and the diabatic $^2A_1$ and $^2B_2$ states, as well as the coupling, by fitting the data points produced from the main CI calculation at each nuclear geometry. The global representation of the adiabatic 1 $^2A'$ surface is then defined as the lower eigenvalue obtained by diagonalizing the 2×2 Hamiltonian matrix of the global representations of the diabatic surfaces and coupling. The 1 $^2A'$ surface will be used for calculations on DEA via the $^2A_1$ (1 $^2A'$) Feshbach resonance, because in that case the conical intersection is not expected to play a large role in the dyamics, and therefore the adiabatic basis is sufficient. (The corresponding vector potential is not included.) The diabatic surfaces and coupling are used to calculate cross sections for DEA via the higher-energy $^2B_2$ (2 $^2A'$) state.

The constructed global representations of the diabatic $^2A_1$ and $^2B_2$ and the adiabatic $^2B_1$ and 1 $^2A'$ surfaces include the errors that we have already mentioned: the three-body asymptotes are too high, and the two-body asymptote of the diabatic $^2A_1$ surface in the H_2+O^- arrangement is too low. In order to fix these errors, we combined these global representations with other global surfaces designed to reproduce the correct behavior in the region in question. In each case a single patching surface is combined with a single CI surface such that the final surface reflects the correct behavior. The surfaces are combined by taking either the higher-energy of the two surfaces (for the $^2A_1$ patching) or the lower-energy of the two surfaces (for the three-body patching), and smoothing the resulting cusps with a simple algebraic formula.

The patching surface for the $^2A_1$ diabatic state must correlate to the proper $H_2(1\sigma_g 1\sigma_u)+O^-$ asymptote of this state. We perform another CI calculation that correlates to this asymptote, and construct a global patching surface from the results, using the combined analytic fit + spline technique we employed for the resonance surfaces. The patching surfaces for the three-body asymptotes of the adiabatic $^2B_1$ and 1 $^2A'$ surfaces, as well as that of the diabatic $^2B_2$ surface, take the form of a simple analytic potential.

The diabatization of the 1 and 2 $^2A'$ adiabatic CI roots is a requirement dictated by the nuclear dynamics calculations. In the adiabatic basis, there are singular derivative couplings near the conical intersection between the 1 and 2 $^2A'$ surfaces. We have not calculated these couplings from our CI wave functions, and in preparation for dynamics calculations on the coupled surfaces, we therefore perform a diabatization upon the 1 and 2 $^2A'$ CI roots to produce the set of diabatic $^2A_1$ and $^2B_2$ curves and the accompanying coupling potential.

In Ref.[25], we described how a full characterization of the manifold of Feshbach resonances must also include a $^2B_2$ shape resonance whose potential-energy curve intersects that of the $^2B_2$ Feshbach resonance in branch-point fashion. We do not include this $^2B_2$ shape-Feshbach intersection, and instead define a single surface which interpolates between the two sheets within the three-body breakup region. Therefore, the nuclear dynamics on this surface is unlikely to accurately represent the dynamics leading to three-body breakup. The results that we will present in paper II indicate that three-body breakup probably comprises a large component of the cross section for dissociative attachment via the $^2B_2$ state.

A. Orbital basis

We constructed a single orbital basis for all the CI calculations on the resonances. We began by augmenting the contracted Gaussian basis of Gil *et al.* [19] with the following additional Gaussian functions: on the hydrogens, two s functions with exponents 0.08 and 0.0333, and two p functions with exponents 0.2 and 0.05; on the oxygen, one s function with exponent 0.0316, and one p function with exponent 0.254. The basis comprised 77 contracted Gaussians total.

We first obtained an orbital basis by performing a symmetry-restricted SCF calculation on the $^2B_1$ resonance, which yielded the $1a_1$, $2a_1$, $1b_2$, $3a_1$, $1b_1$, and $4a_1$ orbitals, labeled $1a'$, $2a'$, $3a'$, $4a'$, $1a''$, and $5a'$ in C_s symmetries. This SCF calculation is bound, i.e., it cannot decay to H_2O+e^- by a symmetry-conserving rotation among the orbitals, because the $1b_1$ orbital is restricted to be singly occupied. The same statement is not true of the other resonances, which are described by a hole in an a' orbital, and therefore we were forced to use this SCF orbital basis for CI calculations on all three resonances, not just $^2B_1$.

These SCF orbitals have avoided crossings (see the graph in the EPAPS archive[41]). When the resonance is

fully dissociated, i.e., in the arrangement O^-+H+H, the $4a_1$ ($5a'$) SCF orbital is best described as $\sqrt{1/2}(\Psi_{H_a 1s} + \Psi_{H_b 1s})$, i.e., the bonding combination of the two hydrogen $1s$ orbitals. These $1s$ orbitals are more similar to the hydride $1s$ orbital than to the hydrogen $1s$ orbital. As the hydrogens are brought closer, the energy of this orbital decreases and eventually crosses the $3a_1$ ($4a'$) and $2b_2$ ($3a'$) orbitals. At finite O^-+H_2 separation, these crossings are avoided. There are avoided crossings between the $3a'$ and $4a'$ ($3a_1$ and $4a_1$) orbitals near θ_{HOH}=48°, and between the $4a'$ and $5a'$ ($4a_1$ and $2b_2$) orbitals near θ_{HOH}=61°. In C_{2v} geometries (e.g., r_1=r_2=7.0a_0) the crossing between the $4a_1$ and $2b_2$ orbital is an actual crossing.

In the definition of the multielectron configuration space that we use for the CI calculation, we treat the $4a_1$ ($5a'$) orbital differently from the $3a_1$ or $2b_2$ orbitals. Thus, it was useful to define a "diabatic" $4a_1$ orbital whose energy smoothly crosses that of the others and is continuous in character. To this end, we performed a rotation among these three orbitals wherein we replaced the oxygen nucleus with an uncharged center, by obtaining the lowest eigenvalue of the H_2^+ Hamiltonian within the space of the $3a_1$, $4a_1$, and $2b_2$ orbitals. The ground state eigenvector of this calculation was defined as the diabatic $4a_1$ orbital, and its complement as the diabatic $3a_1$ and $2b_2$ orbitals. The $4a_1$ diabatic orbital is thus the "H_2-like" orbital. Fortuitously, this rotation leaves the $4a_1$ orbital virtually unchanged at the equilibrium geometry of the neutral. In the OH+H^- asymptote, the $4a_1$ orbital is also left unchanged as the hydride $1s$. The expectation of the Fock operator upon this diabatic $4a_1$ orbital (plotted in the EPAPS archive[41]) passes smoothly through the avoided crossings at θ_{HOH} = 48° and 61°. We used this rotated SCF basis for CI calculations on the three resonances, and in the description of these calculations below, the notation "$4a_1$" refers to the diabatic $4a_1$ orbital.

B. Main CI calculation

The main configuration-interaction (CI) calculation on the three Feshbach resonances employs a configuration space that is restricted to the configurations which contribute most to the resonances under study. This space was defined by the three resonance configurations $[H_2O]1b_1^{-1}4a_1^2$, $[H_2O]3a_1^{-1}4a_1^2$, and $[H_2O]1b_2^{-1}4a_1^2$, plus all singles and doubles into the virtual space, with the $1a_1$ orbital restricted to be doubly occupied. Thus, we excluded from the configuration space all references wherein the combined occupancy of ($1b_2$ $3a_1$ $1b_1$) was six. This restriction excludes configurations of the form $[H_2O]n^1$, which correspond to discretized continuum states of H_2O + e^-. The total size of this configuration space is 111792 in A' symmetry, and 106110 in A'' symmetry.

The restriction placed on the configuration space was critical in that it produced the resonance energies as low-

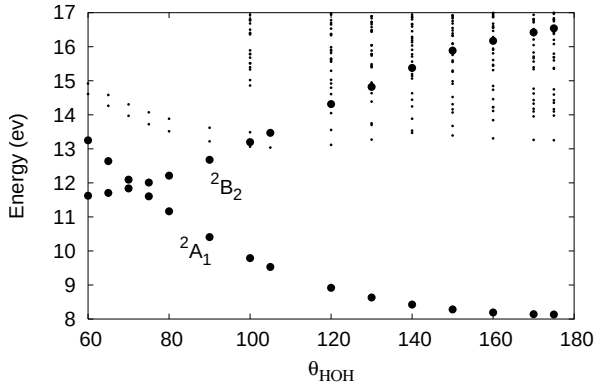

FIG. 14: $^2A'$ roots of the main CI calculation at r_1=r_2=1.81a_0, as a function of bending angle θ.

lying roots of the CI. The resonances were identified by their dominant configuration. The $^2B_1$ ($1\ ^2A''$) energy was found to be always the lowest root of its CI, and the $^2A_1$ ($1\ ^2A'$) state was almost always the lowest root of the CI of that symmetry. Therefore, the energies thereby obtained for these resonances were smoothly varying functions of the nuclear geometry, not suffering from avoided crossings with discretized continuum states. The energy of the $^2B_2$ state rises above discretized continuum states of the type $[H_2O]2b_1^{-1}n^1m^1$ and $[H_2O]3a_1^{-1}n^1m^1$ at certain geometries, namely small OH bond lengths and near-linear H-O-H geometry. However, the resulting avoided crossings were generally observed to be very narrow. The discretized continuum states of excited $[H_2O^*]n^1$ are undercorrelated, relative to the resonance roots, by this multireference, all-doubles treatment, and therefore occur at a higher energy than they would otherwise.

In Fig. 14, we plot the $^2A'$ roots of this configuration-interaction calculation as a function of bending angle θ_{HOH}, at the equilibrium bond lengths r_1=r_2=1.81a_0, showing the behavior of the CI roots near the conical intersection. Also apparent in this figure are the discretized continuum states, many of which lie below the $^2B_2$ resonance root when the bond angle is large.

The orbital and configuration basis for this CI calculation is designed to describe well the resonances at the equilibrium geometry of the neutral and in the two-body dissociation channels. This calculation is not designed to reproduce the three-body asymptotes, and makes a large error in these regions. The $4a_1$ and $2b_2$ orbitals have significant hydride $1s$ character on both hydrogen centers, as opposed to hydrogen $1s$; since there is no relaxation of the hydride $1s$ orbital included in the reference space, the double excitations into the virtual space must play that role, and the three-body asymptotes are therefore undercorrelated and unphysically high in energy. We have not attempted a precise characterization of the CI roots in the three-body breakup region.

We performed these CI calculations at various geometries on a grid based on H-H-O bond angle coordinates

(not H-O-H) r_{HH}, r_{OH}, and θ_{HHO}. We used these coordinates so that the H_2+O^- exit well (along with one of the OH+H^- exit wells) would be well-represented by the spline proceedure we use. In our previous treatment[22] of the $^2B_1$ resonance, we used H-O-H bond-angle coordinates, which led to an unphysically corrugated spline representation of the H_2+O^- well.

For this calculation, we defined a full grid of 23 r points between $1.0a_0$ and $12.0a_0$ and 29 θ points between 1° and 175°. This 23×23×29 grid includes 15341 points. The CI calculations were each performed at roughly 4200 appropriately chosen points on this grid.

The energies of the resonance CI roots at the equilibrium geometry (r_1=r_2=$1.81a_0$, θ=105°) were -76.030888 hartree ($^2B_1$), -75.943508 hartree ($^2A_1$ or 1 $^2A'$), and -75.802877 hartree ($^2B_2$ or 2 $^2A'$).

C. Diabatization

Because the $^2A_1$ and $^2B_2$ states have a conical intersection, and since we have not calculated the derivative couplings between them, a diabatization [44] is required for the nuclear dynamics calculations. Our method for performing this diabatization is an approximate method, based not on the explicit minimization of first-derivative matrix elements[45, 46, 47, 48, 49] but upon the diagonalization of a property [50] to obtain smoothly behaved diabatic states. Our technique is thus analagous to a diabatization via the diagonalization of the dipole operator between states which undergo a charge-transfer avoided crossing [51], or the diagonalization of the l_z angular momentum operator between adiabatic states which have a Σ-Π conical intersection at linear nuclear geometry[38, 52].

The property we use for our diabatization is a symmetry operation—a reflection perpendicular to the molecular plane—which is already diagonal in the adiabatic basis both in C_{2v} geometries and in the asymptotic OH+H arrangement channel. In C_{2v} geometries, this reflection is that defined by the plane that contains the C_{2v} axis, and that is perpendicular to the molecular plane. In such geometries, the $^2A_1$ state is an eigenfunction of this symmetry operation with a eigenvalue of +1 with respect to this reflection, and the $^2B_2$ state has a eigenvalue -1. In the asymptotic OH+H arrangement, this reflection is defined by the plane perpendicular to the OH axis (which again is perpendicular to the molecular plane) that crosses through the oxygen nucleus. In these geometries, the matrix representation of the reflection operator in the basis of these states is diagonal, with the 1 $^2A'$ state, which correlates to H^-+OH($^2\Pi$), having a positive diagonal matrix element, and the 2 $^2A'$ state, which correlates to H^-+OH($^2\Sigma$), having a slightly negative diagonal matrix element.

In Fig. 15, we show the reflection plane for one C_{2v} geometry and for one geometry approaching the H^-+OH arrangement. The reflection plane is that plane that

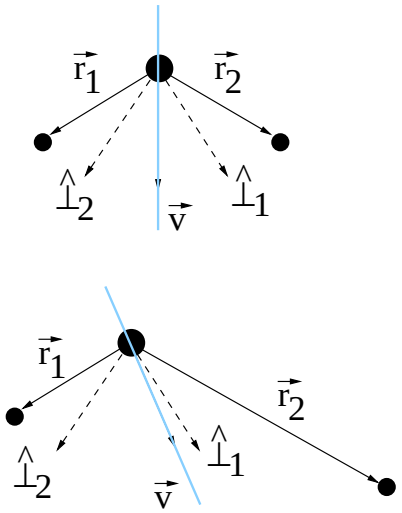

FIG. 15: Vectors involved in defining the reflection operator whose diagonalization provides the $^2A_1$ and $^2B_2$ diabatic states from the 1 and 2 $^2A'$ adiabatic states. The reflection plane is marked by a wide blue (grey) line and contains the vector $\vec{v}$.

contains the vector $\vec{v}$ and which is perpendicular to the molecular plane. The vector $\vec{v}$ is a weighted sum of the unit vectors $\widehat{\perp_1}$ and $\widehat{\perp_2}$. These vectors are defined as the unit vectors that are perpendicular to the corresponding OH bond vectors $\vec{r_1}$ and $\vec{r_2}$, and that are contained in the HOH bond angle. The expression for $\vec{v}$ is

$$\vec{v} = \exp(-r_1/r_0)\widehat{\perp_2} + \exp(-r_2/r_0)\widehat{\perp_1}, \qquad (10)$$

where the length parameter r_0 is 1 bohr. This value was chosen on the basis of the dimensions of the current molecular system, and by inspecting the continuity of the diabatic potential-energy surfaces produced.

D. CI calculation for the ground state potential surface

The Born-Oppenheimer potential-energy surface for the neutral molecule is required for the nuclear dynamics calculations, and to set the zero of energy for the dissociative attachment cross sections thereby produced.

For the calculation of the neutral potential surface, we followed a prescription similar to that used in generating the resonance surfaces. An SCF calculation on the neutral was performed, followed by a configuration-interaction calculation with all singles and doubles from the SCF configuration, keeping the $1a_1$ orbital doubly occupied. The size of this CI calculation is 22215 configurations in C_{2v} symmetry.

For the neutral, we used the physical H-O-H bond angle coordinates and a grid defined by r_{OH}={1.41, 1.61, 1.81, 2.01, 2.21, 2.41, 2.61, 3.01, 3.41 a_0}, and θ={60, 75, 90, 105, 120, 135, 150, 165°}. The CI calculation was performed on each point on this grid.

The energy of the neutral CI calculation at the equilibrium geometry (r_1=r_2=1.81a_0, θ=105°) was -76.2900969 hartree, yielding vertical excitation energies for the resonances of 7.054, 9.431, and 13.258eV. (No zero-point energy is included.)

E. Global representation

To construct a global representation of these five CI potential-energy surfaces—the $^2B_1$, the diabatic $^2A_1$ and $^2B_2$, the patching $^2A_1$ surface, and the ground state surface—a reference potential was first fit to the data, then subtracted from the computed points; the remainder was then fit with three-dimensional cubic splines. The sum of the reference fit plus splined remainder comprises the global fit, which coincides exactly with the calculated points.

The functional forms of the reference potential V_{res} for the four resonance curves and V_{neut} for the neutral are given in the EPAPS archive[41]. Root-mean-square errors of each fit were on the order of 0.1eV.

The errors of each of the analytic fits were fit to cubic splines. Since we did not calculate the full grid of points, a multi-step splining proceedure was required. First, a series of one-dimensional splines, in the θ_{HHO} direction and then along the r_{HH} and r_{OH} directions, was performed to obtain the splined error at the remaining grid points. Second, the full grid of data thus constructed was fit to three-dimensional cubic splines, and added to the analytic fit to obtain the global representation. This proceedure yields the spline surface V_S. The global representation is $V_{res} + V_S$ for the resonances or $V_{neut} + V_S$ for the neutral.

F. Representation of electronic coupling term and transformation of width to diabatic basis

The electronic coupling matrix element between the $^2A_1$ and $^2B_2$ states was represented by a fit to a polynomial times Gaussian expansion in a rotated coordinate system. The explicit form can be found in the EPAPS archive[41]. The RMS error of this fit was 0.05eV.

This global fit of the coupling matrix element has a small remainder. Thus, while the diabatic $^2A_1$ and $^2B_2$ surfaces pass exactly through the calculated points, the coupling surface, and thus the adiabatic surfaces obtained by a diagonalization of the electronic Hamiltonian thereby constructed, do not do so precisely.

G. Patching of the surfaces

The potential-energy surfaces constructed from the main CI calculation appear to reproduce the known features and all but one of the two-body asymptotes of the physical system, without recourse to an overall vertical adjustment in the relative position of the neutral an anion curves, or any other ad hoc adjustment. However, there are two regions in which the current configuration interaction treatment fails to reproduce the physical energetics: for the high-energy $H_2(\sigma_g\sigma_u)$ $^3\Sigma_u$ + O^- asymptote of the 2 $^2A'$ ($^2A_1$) surface, and in the three-body breakup region for all three resonances.

Since the goal of the present study is to present the most physically accurate theoretical treatment of dissociative electron attachment within the local complex potential model, we correct these flaws in the surfaces by employing a patching procedure. In both cases a second surface with the desired characteristics is constructed and patched to the errant area. This patching is performed on the global fits V_{res}+V_S, not upon the original data points. The patching is performed by taking either the maximum of the original and the patching surface (for the diabatic $^2A_1$ surface), or the minimum (for the three-body asymptotes), and smoothing the resultant cusps with a simple mathematical formula. This formula perserves the surfaces identically in the unpatched regions, and is described below.

1. $^2A_1$ patching surface

All three roots of the main CI calculation correlate to H_2+O^- in that arrangement channel. However, the correct asymptote of the 2 $^2A'$ state in that arrangement is $H_2(1\sigma_g1\sigma_u)$+O^- [25]. Therefore, we performed an additional CI calculation that correlates to this state in that arrangment, and patched this surface to the diabatic $^2A_1$ surface produced from the main CI, thereby correcting it. The diabatic $^2B_2$ surface is left unchanged.

The Gaussian basis and orbitals for this CI were exactly the same as those for the main CI, including the rotation of the $4a_1$ orbital; the only difference was the choice of configurations. We included all single and double excitations from the configuration $[H_2O]4a_1^1$, keeping the $1a_1$ orbital doubly occupied, and the $4a_1$ orbital never doubly occupied. We took the lowest root of this CI. In the O+H_2 arrangement, the (diabatic) $4a_1$ orbital correlates to the H_2 $1\sigma_g$ orbital, and therefore the lowest root is O^-+H_2 ($1\sigma_g1\sigma_u$). Elsewhere, the lowest root corresponds to a discretized continuum state of H_2O+e^-, and lies below the diabatic $^2A_1$ surface. We performed this calculation on the same grid as the main CI calculation. We constructed a global representation of the patching surface employing our function V_{res} and a splined residual V_S, just as we did for the resonance surfaces.

This surface and the diabatic $^2A_1$ surface intersect, and the upper surface contains the proper asymptotes for the physical $^2A_1$ surface. It also contains cusps where the surfaces intersect. These cusps were smoothed by the following prescription. Given the separation ΔE and the

average $\overline{E}$ of these two surfaces,

$$\begin{aligned} \Delta E &= |E_{A_1} - E_{patching}| \\ \overline{E} &= (E_{A_1} + E_{patching})/2, \end{aligned} \tag{11}$$

and a geometry-dependent minimum separation A (in eV) defined as

$$A = 0.5 + 12\exp(-2r_{HH}/3 + 1), \tag{12}$$

the patched $^2A_1$ surface was obtained via

$$E_{A_1} \longrightarrow \begin{cases} \overline{E} + \frac{A}{2-\sqrt{2}} - \sqrt{\frac{A^2}{(2\sqrt{2}-2)^2} - (\frac{\Delta E}{2})^2} & \Delta E \leq \frac{A}{2-\sqrt{2}} \\ \max(E_{A_1}, E_{patching}) & \Delta E \geq \frac{A}{2-\sqrt{2}}. \end{cases} \tag{13}$$

2. Three-body asymptote patching

In order to patch the three-body asymptotes of the constructed global representations, we defined the following two functions of the OH bond lengths r_1 and r_2:

$$\begin{aligned} p_{low}(x) &= 8.4287 + 5.8739\exp\left[-1.4838\,(x - 1.81)\right] \\ p_{high}(x) &= 10.7140 + 3.5886\exp\left[-2.4287\,(x - 1.81)\right] \\ x &= \min(r_1, r_2), \end{aligned} \tag{14}$$

in eV, which functions have the same gradient as the $^2B_2$ surface in the symmetric stretch coordinate but are 1.5eV above it at the equilibrium geometry of the neutral. In the three-body breakup region, these functions approach the values of their constant terms, which are chosen to represent the physical asymptotes of the system.

The function p_{low} is used to patch the asymptotes of the $^2B_1$ and the 1 $^2A'$ surfaces. The value of its constant term, 8.43eV, is in-between the asymptotes H^-+H+O^- at 8.75eV and H+H+O^- at 8.04eV. While, as discussed in Ref. [25], the proper asymptote of these adiabatic electronic states is the lower of these, the higher may be reached by an excursion into the OH+H^- two-body breakup channel that does not rigorously follow the adiabatic state in becoming H^-+H+O. Therefore, we choose a compromise between these values to represent the physical system. A more accurate treatment would use two surfaces, but we expect the present treatment to be sufficient for determining the two-body DEA cross sections.

The function p_{high} is used to patch the diabatic $^2B_2$ surface. Its asymptote is chosen as the energy of H^-+H+O(^1D). Unlike the $^2B_1$ and 1 $^2A'$ surfaces, the $^2B_2$ (2 $^2A'$) adiabatic surface is inherently double-valued within the inner regions of nuclear configuration space, and has two proper three-body asymptotes; H+H+O^- is the other asymptote. We have not attempted to characterize the full double-valued $^2B_2$ surface. The patching surface p_{high} corrects the $^2B_2$ three-body asymptote to the higher of its two physical values, in order to reproduce the OH($^2\Sigma$)+H^- two-body asymptote accurately. Therefore, the repulsive wall in the H_2+O^- potential well extends above its physical value. It is hoped that this treatment does not alter the dynamics leading to the two-body dissociation channels to a significant degree.

We combine the functions p_{high} and p_{low} with the resonance surfaces using the same equation, Eq.(13), as we used for the $^2A_1$ patching, with a constant value of A=1.0eV.

H. Transformation of width to diabatic basis

In order to transform the width surfaces produced from the scattering calculations, which are constructed in the adiabatic 1 $^2A'$ and 2 $^2A'$ basis, to the diabatic basis, the adiabatic-to-diabatic transformation matrix was constructed using the *patched* diabatic $^2A_1$ surface and the coupling calculated from the original diabatization of the unpatched surface. This adiabatic-to-diabatic transformation matrix is therefore different from the transpose of the one that diabatized the adiabatic states from the main CI calculation. The diabatic width surfaces are defined as

$$\begin{pmatrix} \Gamma_{^2\mathrm{A}_1} & \Gamma_{\mathrm{C}} \\ \Gamma_{\mathrm{C}} & \Gamma_{^2\mathrm{B}_2} \end{pmatrix} = U^T \begin{pmatrix} \Gamma_{1\ ^2\mathrm{A}'} & 0 \\ 0 & \Gamma_{2\ ^2\mathrm{A}'} \end{pmatrix} U, \tag{15}$$

with the adiabatic-to-diabatic transformation matrix U expressed in terms of the angle θ',

$$U = \begin{pmatrix} \cos(\frac{\theta'}{2}) & \sin(\frac{\theta'}{2}) \\ -\sin(\frac{\theta'}{2}) & \cos(\frac{\theta'}{2}) \end{pmatrix}, \tag{16}$$

which is defined in terms of the patched surface $V_{^2\mathrm{A}'_1}$ as

$$\cot(\theta') = \frac{V_{^2\mathrm{A}'_1} - V_{^2\mathrm{B}_2}}{2\mathrm{C}}. \tag{17}$$

This angle θ' is different than the original angle θ that diagonalized the reflection operator,

$$\cot(\theta) = \frac{V_{^2\mathrm{A}_1} - V_{^2\mathrm{B}_2}}{2\mathrm{C}}, \tag{18}$$

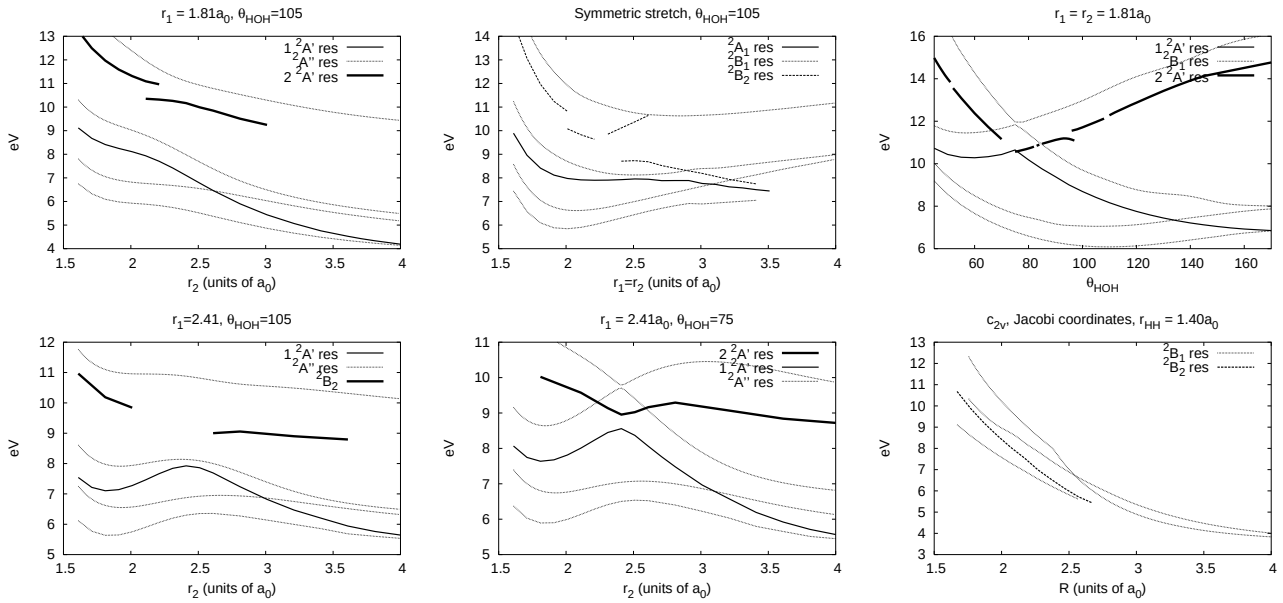

FIG. 16: Comparison of scattering calculations and CI results along various cuts. Bold lines: results of scattering calculations; thin lines, CI results.

where $V_{^2A_1}$ is the original unpatched diabatic $^2A_1$ surface. In particular, in the O^-+H_2 asymptote, the patching vastly increases the difference between the $^2A_1$ and $^2B_2$ surfaces, and thus the new adiabatic-to-diabatic transformation matrix is nearly unity there.

I. Comparison with complex Kohn results

The results of the CI calculations are compared with the resonance locations obtained from the complex Kohn calculation, along various cuts, in Fig. 16. In most cases this comparison is quite favorable, although some differences are apparent. These results are presented in terms of the original, unpatched CI surfaces.

The top three cuts, which each contain the equilibrium geometry of the neutral, are in excellent agreement, except for the 2 $^2A'$ surface for the symmetric stretch cut. Along this cut, the $^2B_2$ resonance has branched into the two components of the double-valued $^2B_2$ shape-Feshbach state, as discussed in Ref. [25].

We include the cuts at r_1=2.41a_0 in Fig. 16 because these geometries are relevant to the wavepacket dynamics on the 2 $^2A'$ surface. The gradient of the real component of that surface, as well as the behavior of the imaginary component, takes the propagated wavepacket through these cuts. The cut at r_1=2.41a_0, θ_{HOH}=75° is near the conical intersection. Along this cut, the behavior of the CI surfaces mirrors the behavior of the Kohn resonances, though the agreement is not as good at θ_{HOH}=105°.

VI. DESCRIPTION OF THE COMPLEX POTENTIAL SURFACES

Several views of the diabatic surfaces can be found in the EPAPS archive[41]. Here we show one in the vicinity of the conical intersection, and then focus on the adiabatic surfaces only.

A. Views of the conical intersection

A plot of the conical intersection is shown in Fig. 17. In this figure, the symmetric stretch coordinate is held constant at $r_1 + r_2$=3.62a_0; we see one cut of the potential-energy surface that intersects the conical intersection seam at a point, at a bond angle of approximately θ_{HOH}=72°.

B. Energetics of the adiabatic surfaces

The real parts of the resonance surfaces $V_{res} + V_S$ with patching are plotted in Fig. 18, fixing the bond lengths at their equilibrium values and varying the bond angle. The initial state starts at θ_{HOH}=104.5°, at which geometry the resonances are 6.63, 9.01, and 12.83eV above the ground vibrational state of the neutral. The conical intersection is apparent at approximately θ_{HOH}=76°, where the $^2A_1$ and $^2B_2$ surfaces intersect. The 1 $^2A'$ surface is plotted separately and is lower than the diabatic surfaces near the conical intersection. This is a consequence of the three-body patching proceedure and the fact that differ-

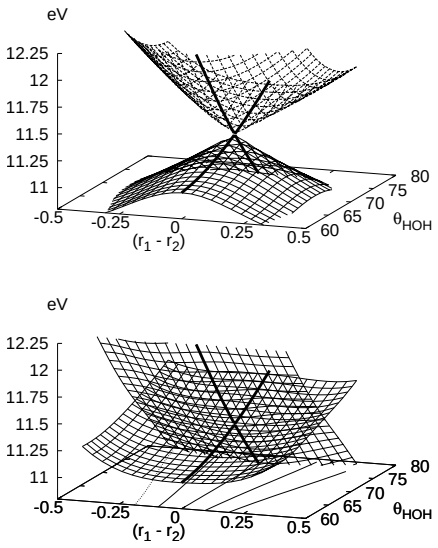

FIG. 17: Cut of conical intersection at $r_1 + r_2$=3.62a_0: adiabatic representation, top; diabatized surfaces and coupling, bottom. Top, values of 1 and 2 $^2A'$ potential surfaces as constructed from global representations $V_{res} + V_S$ of diabatic $^2A_1$ and $^2B_2$ surfaces and coupling. The potentials are plotted with respect to asymmetric stretch, units of bohr, and bending angle in degrees. The $^2A_1$ and $^2B_2$ surfaces along C_{2v} geometry (r_1=r_2) are marked with bold lines. Bottom, fitted diabatized surfaces. The coupling is plotted as contours at bottom, contours every 0.25eV.

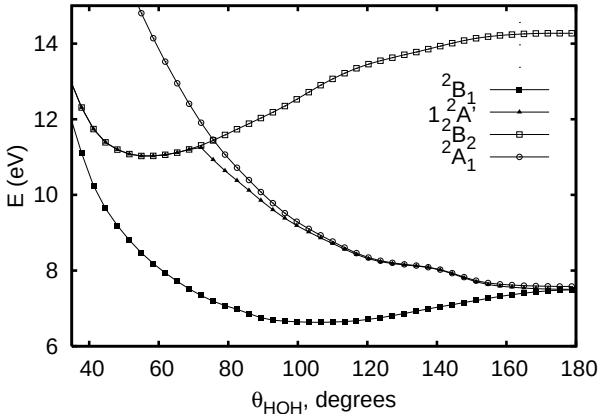

FIG. 18: Potential-energy curves of calculated Feshbach resonances at r_1=r_2=1.81a_0, as constructed by global representation.

ent functions p_{high} and p_{low} are used to patch the 1 $^2A'$ and $^2B_2$ surfaces. The patching of the $^2B_2$ surface is apparent as the slight downward kink of the surface near 115°, at the edge of the Franck-Condon region of the neutral. The bump in the 1 $^2A'$ and $^2A_1$ surfaces near 140° is a localized artifact of the spline which thwarted removal.

The vertical transition energy for the $^2B_1$ state is very near the experimental peak maximum for DEA via this resonance, while the vertical transition energies for the $^2A_1$ and $^2B_2$ states exceed the experimental DEA peak positions by ∼0.4eV and ∼1eV, respectively. We must point out, however, that the location of the experimental peaks in the DEA cross section do not necessarily coincide with the vertical transition energies, especially for the upper states with their shorter lifetimes. As we will see in paper II, the vertical transition energies of the upper resonance states are probably closer to their appropriate physical values than than these comparisons would suggest.

Globally, these potential-energy surfaces appear to reproduce the essential energetics of the underlying physical states. Only in the case of the three-body breakup region is this agreement the result of an *ad hoc* procedure; elsewhere, the potential-energy surfaces represent the results of *ab initio* calculations. In the case of the two-body asymptotes, we have been fortunate to obtain very good agreement with the proper energetics. The energetics of the system of three coupled Feshbach resonances as calculated is summarized in Fig. 19. On the left of this figure are the accepted values for the differences in internal energy among each of these species, obtained from Refs.[53, 54, 55, 56, 57, 58, 59]. On the right are the results of the present calculations. The three-body asymptotes listed there correspond to the unpatched values of the configuration-interaction surfaces at the geometry $(r_1, r_2, \theta) = (10.0a_0, 10.0a_0, 60°)$.

C. Asymptotes of the adiabatic surfaces

The two-body asymptotes of the potential-energy surfaces are plotted in Fig. 20 and compared with benchmark theoretical calculations on the diatomic fragments. The dots in this figure represent the values of the global representations of the potential-energy surfaces evaluated along the cut in Jacobi coordinates at R=10.0a_0, γ=90°. Also plotted in this figure are the values of benchmark calculations for the diatomic H_2 [61] and OH (X $^2\Pi$) [60] fragments, which are shifted so that their zero-point energies lie at the accepted energy above our calculated ground vibrational state energy of neutral H_2O; the solid horizontal lines represent the accepted energy of the three-body channels, again shifted to correspond to our ground state H_2O energy. The theoretical calculations of Chu, Yoshimine and Liu [60] slightly underestimate the true dissociation energy of OH (X $^2\Pi$) and ($^2\Sigma$). As is clear from the comparison with these benchmark calculations, the energetics of the two-body asymptotes of these anion surfaces are reproduced extremely well by our calculations. The ground vibrational state of each agrees with the accepted value to within 0.08eV. The three-body asymptotes have been adjusted by the patch-

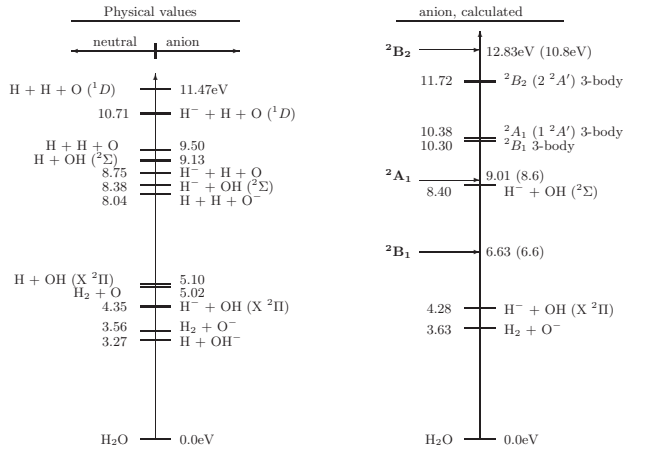

FIG. 19: **Left:** physical thresholds[53, 54, 55, 56, 57, 58, 59] of one- and two-body breakup channels, relative to ground state neutral H_2O, relevant to dissociative electron attachment to H_2O. Vibrational ground states where applicable—zero point energies are included. **Right:** results of the present configuration interaction calculations on the anions, relative to the calculated ground vibrational state of the neutral. The vertical transition energies from the ground vibrational state of the neutral to each CI surface are marked with arrows, with experimental peak maxima in parenthesis for comparison. The three-body asymptotes labeled in the right panel correspond to values of global fits of potential-energy surfaces at (r_1, r_2, θ)=($10.0a_0$, $10.0a_0$, 60°).

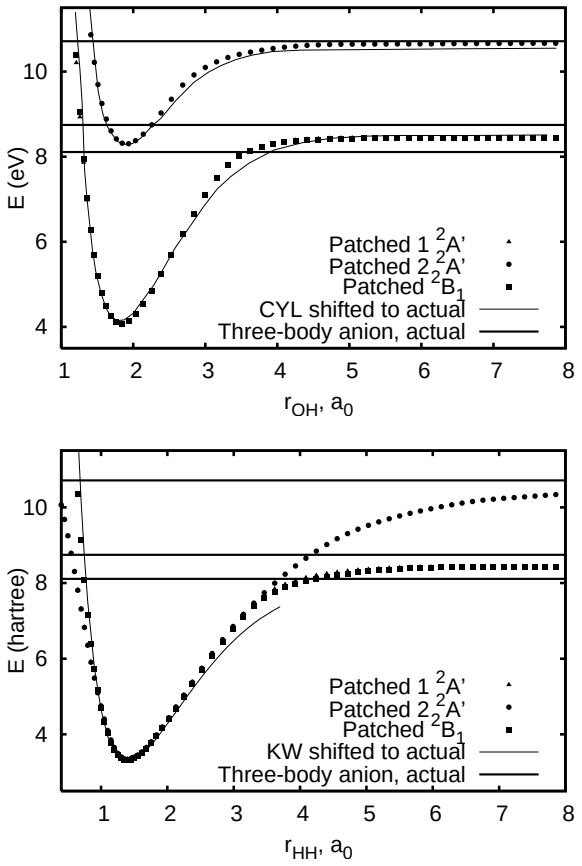

FIG. 20: Diatomic potential curve in OH - H asymptote (top) or H_2 - O asymptote (bottom) of calculated Feshbach resonance curves at R=$10.0a_0$ (dots); benchmark theoretical calculations on OH ($^2\Pi$ / $^2\Sigma$) [60] and H_2 [61] (thin lines) and proper three-body asymptotes (thick lines), with zero point energy oriented relative to our calculated ground state H_2O zero point energy by accepted values.

ing procedure to correspond with the appropriate values.

D. Complete views of the complex-valued adiabatic surfaces

Complete views of the global fits of the real and imaginary components of the adiabatic potential-energy surfaces are shown in Figs. 21-23. The real and imaginary components are plotted together with contour lines, as a function of bond length, for various bond angles. For the imaginary component, the contour line nearest zero is bold, and subsequent contour lines depict the magnitude of the imaginary component increasing. The contour lines for the real part, some of which are marked on the perimeter of each panel, correspond to the energy above the ground state H_2O energy as calculated with our neutral H_2O potential-energy surface, with the zero point energy included, and are therefore consistent with Fig. 19.

In the view of the $^2B_1$ surface in Fig. 21, one can see the two OH+H$^-$ channels at bottom right and upper left of each panel. In the bottom row of panels, which show the surface as the bond angle θ_{HOH} is decreased, one can see the potential well which corresponds to the H_2+O$^-$ channel develop along the symmetric stretch diagonal. This channel is the lowest energy asymptote; it reaches below 4eV, as can be seen in the final panel at 15°. The bottoms of the H$^-$+OH wells in the upper panels are above 4eV. Although the OH+H$^-$ well does reach below 4eV in the panels at θ_{HOH}=30° and 15°, it does so only at small OH-H separations, at which geometry there is a local minimum due to the dipole-anion interaction.

The $^2B_1$ resonance energy is relatively flat with bending angle near the equilibrium geometry of the neutral, and this fact is apparent in the similar shape and value of the contour lines at small r_1 and r_2 in Fig. 21 from θ=150° to θ=75°. At θ=45° and beyond, the bending potential becomes repulsive and the contour lines move towards larger r_1 and r_2. The flatness of the bending curve will cause the dissociating wavepacket to make minimal excursions beyond the cut at θ=105°, and in particular, only a very small fragment of the dissociating wavepacket will reach the O$^-$+H_2 potential well at small θ. The imaginary component of the $^2B_1$ surface is small and localized near the Franck-Condon region.

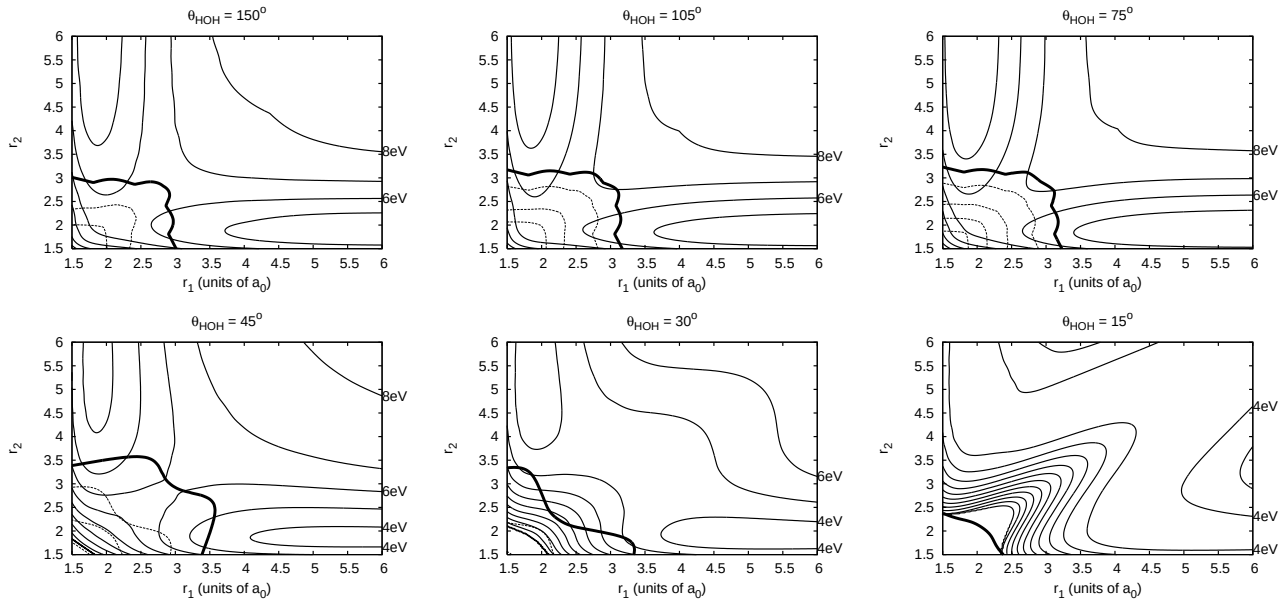

FIG. 21: Complete view of $^2B_1$ surface. Real part: solid contours, 1.0eV spacing. Imaginary part ($\Gamma/2$): dashed contours, 1meV spacing. The bold contour at 1meV is the lowest contour line for the imaginary part.

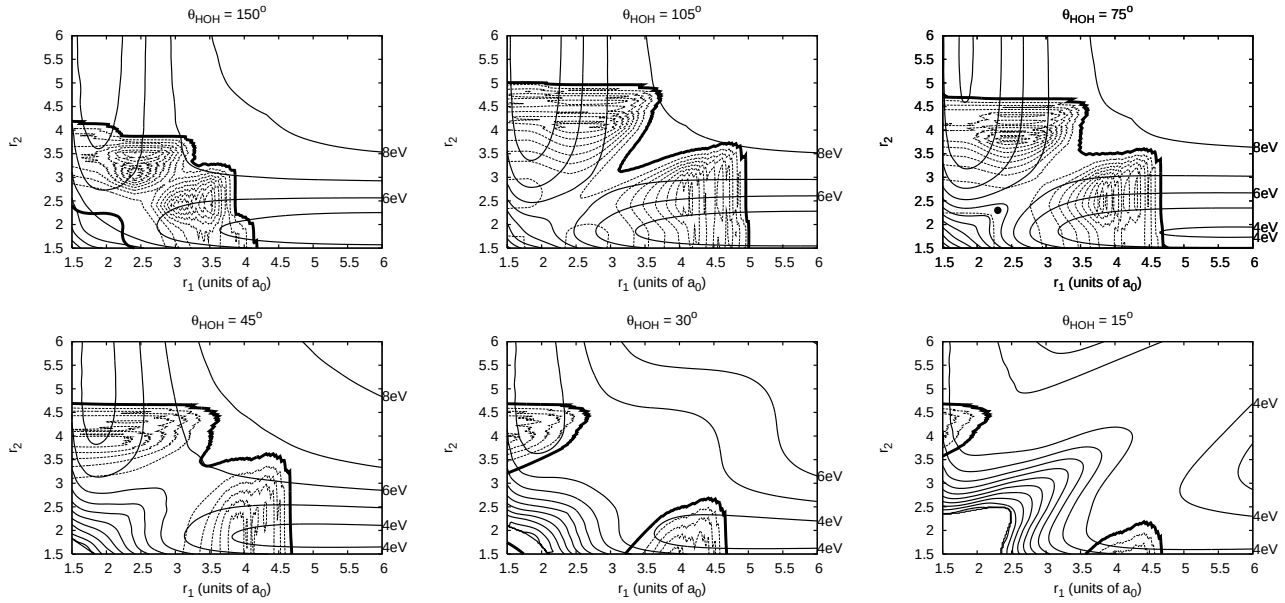

FIG. 22: Complete view of 1 $^2A'$ surface. Real part: solid contours, 1.0eV spacing. Imaginary part ($\Gamma/2$): dashed contours, 5meV spacing. The bold contour at 5meV is the lowest contour line for the imaginary part. Dot, 75°: intersection of conical intersection seam with this cut.

The entire 1 $^2A'$ surface is shown in Fig. 22. The real part of this surface is similar to that of the $^2B_1$ surface, having the same asymptotes, but is everywhere higher (except at linear θ_{HOH}=180° where they are degenerate), and is highest above the $^2B_1$ surface along the conical intersection seam, that intersects this figure at θ_{HOH}=75° at (r_1=r_2=2.3a_0), which point is marked with a dot in the figure. The conical intersection seam is roughly parallel to the grain of the cut, and falls within the plane r_1=r_2. Thus, the dot marks the point where the 1 $^2A'$ surface meets the 2 $^2A'$ surface along this cut. Everywhere else, it is below.

Near the Franck-Condon region of the neutral, the behavior of the 1 $^2A'$ surface with respect to bending angle

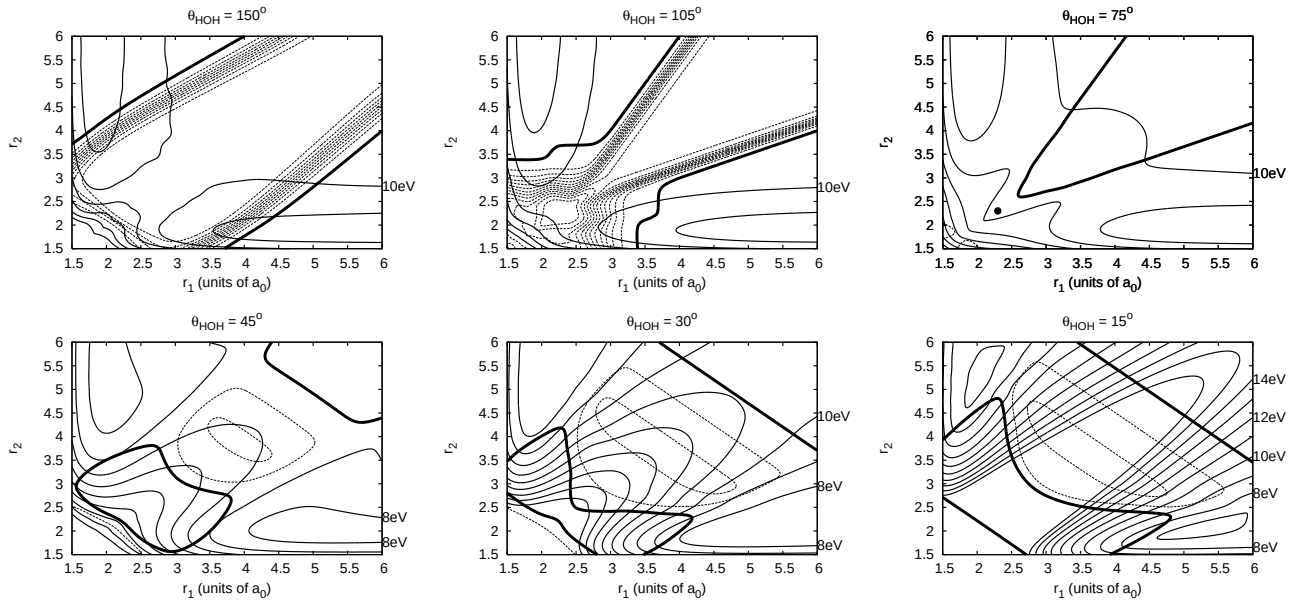

FIG. 23: Complete view of 2 $^2A'$ surface. Real part: solid contours, 1.0eV spacing. Imaginary part ($\Gamma/2$): dashed contours, 10meV spacing. The bold contour at 10meV is the lowest contour line for the imaginary part. Dot, 75°: intersection of conical intersection seam with this cut.

is different from the relatively flat $^2B_1$ surface. In the cut at θ=150° these two surfaces are nearly degenerate, being exactly degenerate at linear geometry. As the bending angle is decreased, however, the 1 $^2A'$ surface rises in energy, and the contour lines in Fig. 22 buckle outward; one such contour line reaches a point at the conical intersection at θ=75°. From this angle, the contour lines near the Franck-Condon region relax slightly downward going to θ=45°, which behavior traces the small well on the 1 $^2A'$ surface apparent in Fig. 18 around θ=55°. At smaller angles, the H_2+O^- potential well develops.

The imaginary component of this state is much different from that of the $^2B_1$ state, being in general higher within the Franck-Condon region, and having the large (0.1eV) peaks in the exit wells just as the resonance becomes bound as H^-+OH. These peaks are a consequence of the A' symmetry of the resonance, as discussed in Ref. [25]. They will lead to a large rate of autodetachment in this channel, and an isotope effect in the cross sections for H_2O versus D_2O that is disproportionate to the entrance amplitude, as discussed in Ref. [23]. They also may portend the breakdown of the LCP model near these geometries, for they indicate that the 1 $^2A'$ state may exist as a virtual state there. We examine this issue more fully in paper II.

The 2 $^2A'$ surface is shown in Fig. 23 and is different from the other surfaces in every region. Its lowest points are along the well of the the H^-+OH($^2\Sigma$) channel where the surface drops to 8eV. This channel has a broader and shallower potential-energy well than the H^-+OH($^2\Pi$) asymptote of the other resonances, with a minimum at approximately r_{OH}=1.95a_0. This surface exhibits a broad plateau in the (r_1, r_2) plane at θ_{HOH}=75° and 10eV. At this angle there is a dimple near the conical intersection at (r_1=r_2=2.3a_0), which is again marked with a dot. There is no H_2+O^- well evident along the symmetric stretch direction at θ_{HOH}=15° because in this arrangement the 2 $^2A'$ state is unbound as H_2 (triplet $1\sigma_g 1\sigma_u$)+O^-; H_2 (triplet $1\sigma_g 1\sigma_u$) has a dissociative potential-energy curve. Thus, the panel at θ_{HOH}=15° shows a cut along the top of this repulsive wall, going up past the last contour line at 16eV; this repulsive wall extends infinitely in the symmetric stretch direction at ever smaller θ_{HOH}. Near the Franck-Condon region, one can see that the real part of the surface is high (∼15eV) at θ_{HOH}=150°, and slopes downward going from panel to panel to θ_{HOH}=75°, as the contour lines near r_1=r_2=1.81a_0 go from being convex to concave. Moving on to the panels at 45°, 30° and 15°, the repulsive wall of $H_2(1\sigma_g 1\sigma_u)$+O^- then quickly develops.

This surface, constructed from the CI calculation, is single-valued, though the physical surface is not. The $^2B_2$ shape resonance curve which intersects that of the $^2B_2$ Feshbach resonance in branch-point fashion[25] has been omitted from the present treatment. The physical 2 $^2A'$ surface contains not only the $H_2(1\sigma_g 1\sigma_u)$+O^- asymptote (overall $^2A_1$ symmetry) at small H-H bond distances, but also the metastable $H_2^-(1\sigma_g^2\ 1\sigma_u)$+O($^1D$) asymptote (overall $^2B_2$ symmetry) as well; the two three-body asymptotes of this state are thus H+H^-+O(^1D) and H+H+O^- (degenerate with 1 $^2A'$). We patch the three-body breakup region of the $^2B_2$ surface to its upper physical asymptote at 10.71eV.

The imaginary component of the 2 $^2A'$ state takes a

large value (∼0.12eV) along the symmetric stretch direction for θ_{HOH}=105° and 150° but otherwise is smaller; its representation is dominated by the interpolation between the large-valued regions and the small-valued regions. In particular, in the H^-+OH ($^2\Sigma$) exit well the imaginary component drops to approximately 0.02eV by (r_1=1.8a_0, r_2=3.5a_0). The interpolation is physical when r_1 or r_2 is small. However, in the three-body channel, we interpolate between physically distinct sheets of the $^2A'$ manifold. Thus, the imaginary component drops from 100meV near the diagonal for $r_1 \approx r_2 > 3.0a_0$ going from θ_{HOH}=105° to θ_{HOH}=75°, but this behavior is unphysical, and corresponds to the interpolation between the two sheets of $^2B_2$ symmetry. The imaginary component remains small along the diagonal going from θ_{HOH}=75° to 45° as the conical intersection is passed and the symmetry of the 2 $^2A'$ state changes from $^2B_2$ to $^2A_1$.

VII. CONCLUSION

We have calculated the potential-energy surfaces necessary for a description of dissociative eletron attachment to H_2O. In paper II, these surfaces are used in a study of the nuclear dynamics in the local complex potential model, and the cross sections for dissociative eletron attachment are calculated.

Acknowledgments

This work was performed under the auspices of the US Department of Energy by the University of California Lawrence Berkeley National Laboratory under Contract DE-AC02-05CH11231 and was supported by the U.S. DOE Office of Basic Energy Sciences, Division of Chemical Sciences.

[1] D. T. Birtwistle and A. Herzenberg, J. Phys. B **4**, 53 (1971).
[2] L. Dube and A. Herzenberg, Phys. Rev. A **20**, 194 (1979).
[3] J. N. Bardsley and J. M. Wadehra, J. Chem. Phys. **78**, 7227 (1983).
[4] T. F. O'Malley and H. S. Taylor, Phys. Rev. **176**, 207 (1968).
[5] T. F. O'Malley, Phys. Rev. **150**, 14 (1966).
[6] D. J. Haxton, T. N. Rescigno, and C. W. McCurdy, Phys. Rev. A **75**, 012711 (2007).
[7] W. N. Lozier, Phys. Rev. **36**, 1417 (1930).
[8] J. Fedor and *et al.*, J. Phys B **39**, 3935 (2006).
[9] I. S. Buchel'nikova, Zh. Eksp. Teor. Fiz. **35**, 1119 (1959).
[10] G. J. Schultz, J. Chem. Phys. **44**, 3856 (1966).
[11] R. N. Compton and L. G. Christophorou, Phys. Rev. **154**, 110 (1967).
[12] C. E. Melton, J. Chem. Phys. **57**, 4218 (1972).
[13] L. Sanche and G. J. Schultz, J. Chem. Phys. **58**, 479 (1972).
[14] S. Trajmar and R. I. Hall, J. Phys. B. **7**, L458 (1974).
[15] D. S. Belič, M. Landau, and R. I. Hall, J. Phys. B. **14**, 175 (1981).
[16] M. G. Curtis and I. C. Walker, J. Chem. Soc. Faraday Trans. **88**, 2805 (1992).
[17] C. R. Claydon, G. A. Segal, and H. S. Taylor, J. Chem. Phys **54**, 3799 (1971).
[18] M. Jungen, J. Vogt, and V. Staemmler, Chem. Phys. **37**, 49 (1979).
[19] T. J. Gil, T. N. Rescigno, C. W. McCurdy, and B. H. Lengsfeld III, Phys. Rev. A **49**, 2642 (1994).
[20] L. A. Morgan, J. Phys. B **31**, 5003 (1998).
[21] J. D. Gorfinkel, L. A. Morgan, and J. Tennyson, J. Phys. B **35**, 543 (2002).
[22] D. J. Haxton, Z. Zhang, C. W. McCurdy, and T. N. Rescigno, Phys. Rev. A **69**, 062713 (2003).
[23] D. J. Haxton, Z. Zhang, H.-D. Meyer, T. N. Rescigno, and C. W. McCurdy, Phys. Rev. A **69**, 062714 (2003).
[24] D. J. Haxton, T. N. Rescigno, and C. W. McCurdy, Phys. Rev. A **73**, 062724 (2006).
[25] D. J. Haxton, T. N. Rescigno, and C. W. McCurdy, Phys. Rev. A **72**, 022705 (2005).
[26] W. Kohn, Phys. Rev. **74**, 1763 (1948).
[27] R. K. Nesbet, Phys. Rev. **175**, 134 (1968).
[28] R. K. Nesbet, Phys. Rev. **179**, 60 (1969).
[29] A. U. Hazi, T. Rescigno, and M. Kurilla, Phys. Rev. A **23**, 1089 (1981).
[30] W. H. Miller and B. M. D. D. J. op de Haar, J. Chem. Phys. **86**, 6213 (1987).
[31] B. I. Schneider and T. N. Rescigno, Phys. Rev. A **47**, 3749 (1988).
[32] J. Z. H. Zhang, S.-I. Chu, and W. H. Miller, J. Chem. Phys. **88**, 6233 (1988).
[33] B. H. Lengsfeld III and T. N. Rescigno, Phys. Rev. A **44**, 2913 (1991).
[34] T. N. Rescigno, C. W. McCurdy, A. E. Orel, and B. H. Lengsfeld III, in *Computational Methods for Electron-Molecule Collisions*, edited by W. M. Huo and F. A. Gianturco (Plenum, New York, 1995).
[35] T. N. Rescigno, B. H. Lengsfeld III, and C. W. McCurdy, in *Modern Electronic Structure Theory*, edited by D. R. Yarkony (World Scientific, Singapore, 1995), vol. 1, pp. 501–588.
[36] H. Feshbach, Ann. Phys. **19**, 287 (1962).
[37] R. G. Newton, *Scattering Theory of Particles and Waves* (Springer-Verlag, New York, 1982), 2nd ed.
[38] R. van Harrevelt and M. C. van Hemert, J. Chem. Phys. **112**, 5777 (2000).
[39] R. A. Kendall, J. T. H. Dunning, and R. J. Harrison, J.

Chem. Phys. **96**, 6796 (1992).
[40] D. Chipman, Theor. Chim. Acta **76**, 73 (1989).
[41] EPAPS Document No. E-PLRAAN-75-005702 for subroutines that generate the real and imaginary components of the constructed potential energy surfaces. For more information on EPAPS, see http://www.aip.org/pubservs/epaps.html.
[42] B. M. Nestmann and S. D. Peyerimhoff, J. Phys. B **23**, L773 (1990).
[43] S.-I. Chu, J. Chem. Phys. **61**, 5389 (1974).
[44] W. Domcke and G. Stock, Adv. Chem. Phys. **100**, 1 (1997).
[45] D. R. Yarkony, J. Chem. Phys. **105**, 10456 (1996).
[46] D. R. Yarkony, J. Phys. Chem. **105**, 6277 (2001).
[47] R. G. Sadygov and D. R. Yarkony, J. Chem. Phys. **109**, 20 (1998).
[48] C. A. Mead, Rev. Mod. Phys. **64**, 51 (1992).
[49] M. Baer, Physics Reports **358**, 75 (2002).
[50] A. Macias and A. Riera, J. Phys. B **11**, L489 (1978).
[51] H.-J. Werner and W. Meyer, J. Chem. Phys. **74**, 5802 (1981).
[52] R. van Harrevelt and M. C. van Hemert, J. Chem. Phys. **114**, 9453 (2001).
[53] P. G. Wilkinson, Astrophys. J. **138**, 778 (1963).
[54] C. Carlone and F. W. Dalby, Can. J. Phys. **47**, 1945 (1969).
[55] B. Russic and *et al.*, J. Phys. Chem. A **106**, 2727 (2002).
[56] G. Herzberg, Phys. Rev. Lett. **23**, 1081 (1969).
[57] J. R. Smith, J. B. Kim, and W. C. Lineberger, Phys. Rev. A **55**, 2036 (1997).
[58] K. R. Lykke, K. K. Murray, and W. C. Lineberger, Phys. Rev. A **43**, 6104 (1991).
[59] C. Valli, C. Blondel, and C. Delsart, Phys. Rev. A **59**, 3809 (1999).
[60] S.-I. Chu, M. Yoshimine, and B. Liu, J. Chem. Phys. **61**, 5389 (1974).
[61] W. Kolos and L. Wolniewicz, J. Chem. Phys. **41**, 3663 (1964).